Mean temperature–velocity relation and a new temperature wall model for compressible laminar and turbulent flows

Xianliang Chen[1,2] ![ORCID], Jianping Gan[1,2] ![ORCID] and Lin Fu[1,3] ![ORCID]

[1]Department of Mathematics and Center for Ocean Research in Hong Kong and Macau (CORE), The Hong Kong University of Science and Technology, Clear Water Bay, Kowloon, Hong Kong, PR China

[2]Department of Ocean Science, The Hong Kong University of Science and Technology, Clear Water Bay, Kowloon, Hong Kong, PR China

[3]Department of Mechanical and Aerospace Engineering, The Hong Kong University of Science and Technology, Clear Water Bay, Kowloon, Hong Kong, PR China

Corresponding author: Lin Fu, linfu@ust.hk

The well-known quadratic temperature–velocity (TV) relation is significant for physical understanding and modelling of compressible wall-bounded turbulence. Meanwhile, there is an increasing interest in employing the TV relation for laminar modelling. In this work, we revisit the TV relation for both laminar and turbulent flows, aiming to explain the success of the TV relation where it works, improve its accuracy where it deviates and relax its limitation as a wall model for accurate temperature prediction. We show that the general recovery factor defined by Zhang *et al.* (*J. Fluid. Mech.*, vol. 739, 2014, pp. 392–440) is not a wall-normal constant in most laminar and turbulent cases. The effective Prandtl number Pr_e is more critical in determining the shape of temperature profiles. The quadratic TV relation systematically deviates for laminar boundary layers irrespective of Mach number and wall boundary conditions. We find a universal distribution of Pr_e, based on which the TV relation can be notably improved, especially for cold-wall cases. For turbulent flows, the TV relation as the wall model can effectively improve the near-wall temperature prediction for cold-wall boundary layer cases, but it involves boundary-layer-edge quantities used in the Reynolds analogy scaling, which hinders the application of the wall model in complex flows. We propose a transformation-based temperature wall model by solving inversely the newly developed temperature transformation of Cheng and Fu (*Phy. Rev. Fluids*, vol. 9, 2024, no. 054610). The dependence on edge quantities is thus removed in the new model and the high accuracy in turbulent temperature prediction is maintained for boundary layer flows.

1. Introduction

The relation between mean temperature and velocity stands as a central fundamental problem in compressible flows research, significant for reliable modelling of high-speed wall-bounded flows (Bradshaw 1977; Cheng *et al.* 2024). The classical relations of Crocco (1932), Busemann (1931) and Walz (1969) suggest that the mean temperature is almost a quadratic function of the mean streamwise velocity, yet these relations only hold for adiabatic flows. A crucial improvement was contributed by Duan & Martín (2011), who introduced a semi-empirical quadratic function of the velocity for turbulent boundary layers. The resulting quadratic temperature–velocity (TV) relation for a calorically perfect gas (CPG) is

$$\bar{T} = T_w + (\bar{T}_r - T_w)\left[C_T \frac{\bar{u}}{\bar{u}_e} + (1 - C_T)\left(\frac{\bar{u}}{\bar{u}_e}\right)^2\right] + (\bar{T}_e - \bar{T}_r)\left(\frac{\bar{u}}{\bar{u}_e}\right)^2, \qquad (1.1a)$$

where $\bar{T}$ and $\bar{u}$ are the mean temperature and velocity; w and e denote wall and boundary layer edge, respectively; $\bar{T}_r = \bar{T}_e + r\bar{u}_e^2/(2c_p)$ is the recovery temperature with r the recovery factor and c_p the isobaric heat capacity; the constant C_T is determined to be 0.8259 for air flows. Equation (1.1) is highly accurate for both adiabatic and diabatic turbulent flat-plate boundary layers, even with high-enthalpy effects (using enthalpy instead; Passiatore *et al.* 2022). Moreover, it works well for turbulent channel and pipe flows if $\bar{u}_e$ and $\bar{T}_e$ are replaced by the centreline counterparts (e.g. Modesti & Pirozzoli 2019). Due to its high accuracy, (1.1) has become a conventional method to examine newly accumulated direct numerical simulation (DNS) data. More importantly, (1.1) enables accurate and efficient recovery of the mean flow and the construction of reliable wall models when combined with velocity transformations, which provides a robust way to model the compressibility effects (Song, Zhang & Xia 2023; Chen *et al.* 2023*a*; Griffin, Fu & Moin 2023; Hasan *et al.* 2024; Chen, Gan & Fu 2024).

An important theoretical work to interpret (1.1*a*) is accomplished by Zhang *et al.* (2014) through introducing the generalised Reynolds analogy (GRA). A critical step is to introduce a general recovery factor r_g, so a counterpart of (1.1*a*) is derived as

$$\bar{T} = T_w + (\bar{T}_{rg,e} - T_w)\frac{\bar{u}}{\bar{u}_e} + (\bar{T}_e - \bar{T}_{rg,e})\left(\frac{\bar{u}}{\bar{u}_e}\right)^2, \qquad (1.1b)$$

where $\bar{T}_{rg,e} = \bar{T}_e + r_{g,e}\bar{u}_e^2/(2c_p)$. Equation (1.1*b*) takes the same form as Walz's equation except for replacing $\bar{T}_r$ with $\bar{T}_{rg,e}$. Furthermore, C_T is recast to be sPr, where $Pr \approx 0.71$ is the Prandtl number and the Reynolds analogy factor s is approximately 1.14 for canonical air flows. Hereafter, (1.1*a*) and (1.1*b*) are referred to collectively as the TV relation without distinctions. Although (1.1) is constructed for turbulent flows, the recent interesting work of Mo & Gao (2024) shows that (1.1) is also applicable to laminar boundary layers, indicating a kind of essential similarity between laminar and turbulent flows. They proceeded to propose a laminar wall model, in combination with velocity scalings, which enables fast and accurate prediction of the skin friction and surface heat flux on a coarse mesh with very low grid density near the wall (wall-normal height of the first grid point off the wall relaxed from 10^{-6} m to 10^{-3} m for their hypersonic cases). This laminar

wall model is also applicable to curved-wall cases where no simple self-similar solutions exist. Nevertheless, the TV relation for laminar flows has not been fully examined in large parameter spaces, compared with their turbulent counterparts. It is therefore the first task of this work to take scrutiny on these TV relations over a wide range of parameters and seek for possible improvements. Moreover, in deriving these TV relations, a crucial assumption is that r_g (or the effective Prandtl number defined later) is a constant independent of wall-normal height. Consequently, two questions naturally arise. (1) Is r_g really a constant in laminar and turbulent flows? And (2) if it is not a constant, why does the quadratic relation still work (or not) in these regions?

The last motivation of this work is from the modelling perspective. Equation (1.1) has been employed for modelling the mean flow within the frameworks of ordinary differential equations (ODEs), Reynolds-averaged Navier–Stokes (RANS) and wall-modelled large eddy simulations (WMLES) (Griffin *et al.* 2023; Hasan *et al.* 2024; Chen *et al.* 2023*b*, 2024). Though notable improvements have been obtained, an obvious limitation of these models is that (1.1) is explicitly dependent on boundary-layer edge values $\bar{u}_e$ and $\bar{T}_e$. Consequently, they cannot be directly used in more complex flow configurations, where the boundary-layer edge cannot be easily determined (Griffin, Fu & Moin 2021*a*). Therefore, we aim to propose an alternative temperature wall model based on newly developed temperature transformations, which excludes the use of boundary-layer edge quantities.

The remaining sections are organised as follows. The TV relation and related parameters are examined in § 2 for both laminar and turbulent flows using wide DNS datasets. We explain the success of the TV relation where it works and improve its accuracy where it deviates. The modelling issues are discussed in § 3, where a new temperature wall model is proposed using recently developed temperature transformations. Finally, concluding discussions are provided in § 4.

2. Results of the TV relations

2.1. *Basic relations of GRA*

For CPG turbulent boundary layers, Zhang *et al.* (2014) define r_g from a GRA relation on the total enthalpy,

$$\bar{H}_g - H_w = c_p \frac{\partial \bar{T}}{\partial \bar{u}}|_w \bar{u}, \tag{2.1}$$

where $\bar{H}$ is the total enthalpy and $\bar{H}_g = c_p \bar{T} + r_g \bar{u}^2/2$ is the general recovery enthalpy. Equation (2.1) is explicitly expressed as

$$\bar{T} + \frac{r_g}{2c_p} \bar{u}^2 - T_w = \frac{\partial \bar{T}}{\partial \bar{u}}|_w \bar{u}, \quad \text{then} \quad r_g = \frac{2c_p}{\bar{u}^2} \left(T_w - \bar{T} + \frac{\partial \bar{T}}{\partial \bar{u}}|_w \bar{u} \right). \tag{2.2a,b}$$

By definition, r_g varies with the wall-normal height y, and can be obtained *a posteriori* using $\bar{T}$ and $\bar{u}$. Zhang *et al.* (2014) further introduce an effective turbulent Prandtl number Pr_e, which relates to r_g as

$$r_g = \frac{c_p}{\bar{u}} \left(\frac{\partial \bar{T}}{\partial \bar{u}}|_w - \frac{1}{Pr_e} \frac{\partial \bar{T}}{\partial \bar{u}} \right) \tag{2.3a}$$

$$\text{or conversely,} \quad \frac{1}{Pr_e} = 1 + \frac{\bar{u}^2}{2c_p} \frac{\partial r_g}{\partial \bar{u}} / \frac{\partial \bar{T}}{\partial \bar{u}}. \tag{2.3b}$$

The combination of (2.2) and (2.3) finally leads to an important ODE for the TV relation,

$$\bar{T} - \frac{\bar{u}}{2}\left(\frac{\partial \bar{T}}{\partial \bar{u}}|_w + \frac{1}{Pr_e}\frac{\partial \bar{T}}{\partial \bar{u}}\right) = T_w, \tag{2.4}$$

which can be solved provided a prescribed distribution of Pr_e, and under the outer boundary condition, $\bar{T}|_{\bar{u}=\bar{u}_e} = \bar{T}_e$. Zhang *et al.* (2014) further assume $Pr_e \approx 1$, which is equivalent to assuming r_g a constant, as seen from (2.3*b*). As a result, the integration of (2.4) leads to the quadratic relation (1.1). The remaining unknown $(\partial \bar{T}/\partial \bar{u})_w$ can be computed from (2.3*a*) at the boundary-layer edge using $r_{g,e}$, and $r_{g,e}$ is related to the analogy factor s as

$$r_g = r_{g,e} = r\left[sPr + (1 - sPr)\Theta\right], \qquad s \equiv \frac{2C_h}{C_f} = \frac{\bar{q}_w \bar{u}_e}{\bar{\tau}_w c_p (\bar{T}_r - T_w)}, \tag{2.5a,b}$$

where the non-dimensional wall temperature $\Theta = (T_w - \bar{T}_e)/(\bar{T}_r - \bar{T}_e)$ is also called the diabatic parameter; C_f and C_h are the coefficients of skin friction and heat transfer, and τ_w and q_w are the wall friction and heat flux. Since s is found to be a robust parameter (Chi & Spalding 1966; Bons 2005; Fu *et al.* 2021), $r_{g,e}$ can be computed *a priori*, so (1.1) can be fully determined. Notably, the original definition of Pr_e by Zhang *et al.* (2014) is based on turbulent fluctuations, which gives Pr_e physical interpretations. The resulting (2.4) provides another way to evaluate Pr_e *a posteriori*, using only $\bar{T}$ and $\bar{u}$ without fluctuation statistics. As will be shown below, such an evaluation from the mean flow is critical to interpret the TV relations and improve modelling.

Interestingly, Wenzel, Gibis & Kloker (2022) (and also Cogo *et al.* (2023)) showed that a form of Eckert number, $Ec = \bar{u}_e^2/[c_p(\bar{T}_r - T_w)]$ for a CPG, is an insightful parameter to account for heat-transfer effects. In fact, we note that Ec can be related to $r_{g,e}$ as

$$Ec^{-1} = \frac{r}{2}(1 - \Theta) = \frac{r - r_{g,e}}{2(1 - sPr)} \quad \text{or} \quad r_{g,e} = r - 2(1 - sPr)Ec^{-1}. \tag{2.6a,b}$$

Since the parameters r, Pr and s are nearly independent of the Mach number Ma and $T_w/\bar{T}_r$, Ec^{-1} and $r_{g,e}$ are essentially equivalent in accommodating heat-transfer effects; Ec^{-1} measures the departure of $r_{g,e}$ from r.

The above GRA relations are also generally applicable to turbulent channel and pipe flows, if all the edge quantities are replaced by the channel/pipe centreline quantities ($\bar{u}_c$, $\bar{T}_c$, $r_{g,c}$, etc.; Modesti & Pirozzoli (2019); Song *et al.* (2022)). Note that (1.1) has been expressed using both the Reynolds-averaged and Favre-averaged variables among literatures. The differences between these two forms are usually minor (e.g. Zhang, Duan & Choudhari (2018)), so the Reynolds average is used here throughout, denoted by overbars. In addition to turbulent flows, Mo & Gao (2024) reformulate the GRA relations for laminar boundary layers. They define r_g the same as in (2.2), and assume r_g a constant, which is mathematically equivalent to $Pr_e = 1$ and leads to exactly the same ODE (2.4) (after enforcing $Pr_e = 1$) for laminar flows. The constant r_g can be obtained from (2.5) and the same quadratic relation (1.1*b*) is arrived. Therefore, the relations (2.2) to (2.5) turn out to be universal for both turbulent and laminar flows, in both boundary layer and channel (and pipe) configurations.

In short, two components are required to solve (2.4) for the TV relation: the first is the wall-normal distribution of Pr_e, which determines the shape of $\bar{T}$; the second is $r_{g,e}$, or equivalently s, which determines the wall boundary condition $(\partial \bar{T}/\partial \bar{u})_w$. Previous models assume constancy of r_g (and Pr_e) for both turbulent and laminar flows, leading to the

quadratic TV relation and temperature wall models. In the following, we carefully examine these assumptions for laminar and turbulent flows, respectively. Both channel flow and flat-plate boundary layers are considered. Although laminar flows are much easier to be resolved than turbulence, we still present the laminar TV results for three reasons. First, as mentioned in § 1, the laminar TV relation can be used to efficiently improve the prediction of C_f and C_h by largely relaxing the near-wall grid density; this strategy for flat plates can be directly applied to curved-wall cases which inhibits simple self-similar solutions (Mo & Gao 2024). Therefore, a comprehensive evaluation on the accuracy of the laminar TV relation is required. Second, Mo & Gao (2024) only studied three severely cold-wall boundary layer cases ($T_w/\bar{T}_r < 0.2$), where r_g has a mild wall-normal variation. Here, we explore a wide parameter space (Ma from 2 to 10 and $T_w/\bar{T}_r$ from 0.1 to 1.6 for boundary layers), and will show that r_g severely differs at different $T_w/\bar{T}_r$ but a universal distribution of Pr_e can be identified. Third, a number of similarities of the TV relation between laminar and turbulent flows will be reported, suggesting some fundamental resemblance between the two flows, as already partly exhibited from their common GRA relations above.

Only CPG air flows are considered. The laminar flow is solved from the Navier–Stokes (NS) equations (detailed later), where the viscosity μ is from Sutherland's law (reference temperature set to 270 K) and a constant $Pr = 0.71$ is adopted throughout. For turbulent cases, elaborated DNS datasets of wide parameter ranges are employed. The factor r for all cases is set to $Pr^{1/3}$.

2.2. *Laminar channel flows*

The compressible NS equations for laminar channel flow degenerate into ODEs,

$$\left(\bar{\mu}\bar{u}_y\right)_y = \bar{p}_x = -\frac{\bar{\tau}_w}{h}, \qquad \bar{\mu}\bar{u}_y^2 + \frac{c_p}{Pr}\left(\bar{\mu}\bar{T}_y\right)_y = 0, \tag{2.7}$$

where the subscript y denotes wall-normal derivatives, $\bar{p}_x$ is the streamwise pressure gradient and h is the channel half-height ($y \in [0, 2h]$). The overbars are retained for consistency in notation. After non-dimensionalisation, the only parameter controlling the shape of the flow is the bulk Mach number Ma_b, measuring the ratio of bulk velocity $\bar{u}_b$ and the wall speed of sound. The Chebyshev collocation point method is adopted to solve (2.7) using $N_y = 201$ grid points, which achieves grid independence.

The temperature profiles at different Ma_b are shown in figure 1(*a*) as a function of the streamwise velocity. The TV relation (1.1) is also displayed with s computed from (2.5*b*), as labelled in the legend. It is shown that even with Ma_b up to 5, (1.1) agrees with the $\bar{T}$ from NS equations very well, which is not widely expected before for laminar channel flows. After attaining the mean flow, r_g is determined by (2.2), as displayed in figure 1(*b*). An immediate observation is that r_g increasingly varies with $\bar{u}$ as Ma_b rises; it changes by over 15 % in the wall-normal direction at $Ma_b = 5$. Also, r_g decreases more rapidly near the wall than in the outer region. Therefore, it seems difficult to trust the results of constancy r_g in § 2.1, so a natural question is why does the TV relation still work?

As noted in § 2.1, Pr_e is more significant than r_g in determining the shape of $\bar{T}$, so we define the counterpart of Pr_e in laminar flows from (2.3) and (2.4), whose physical meaning will be discussed in § 4.1. For convenience of writing, we still use the notation Pr_e, so (2.2) to (2.5) take the same form for both turbulent and laminar flows. From (2.4), Pr_e can be expressed as

$$Pr_e^{-1} = \frac{2(\bar{T} - T_w)/\bar{u} - (\partial\bar{T}/\partial\bar{u})_w}{\partial\bar{T}/\partial\bar{u}}. \tag{2.8}$$
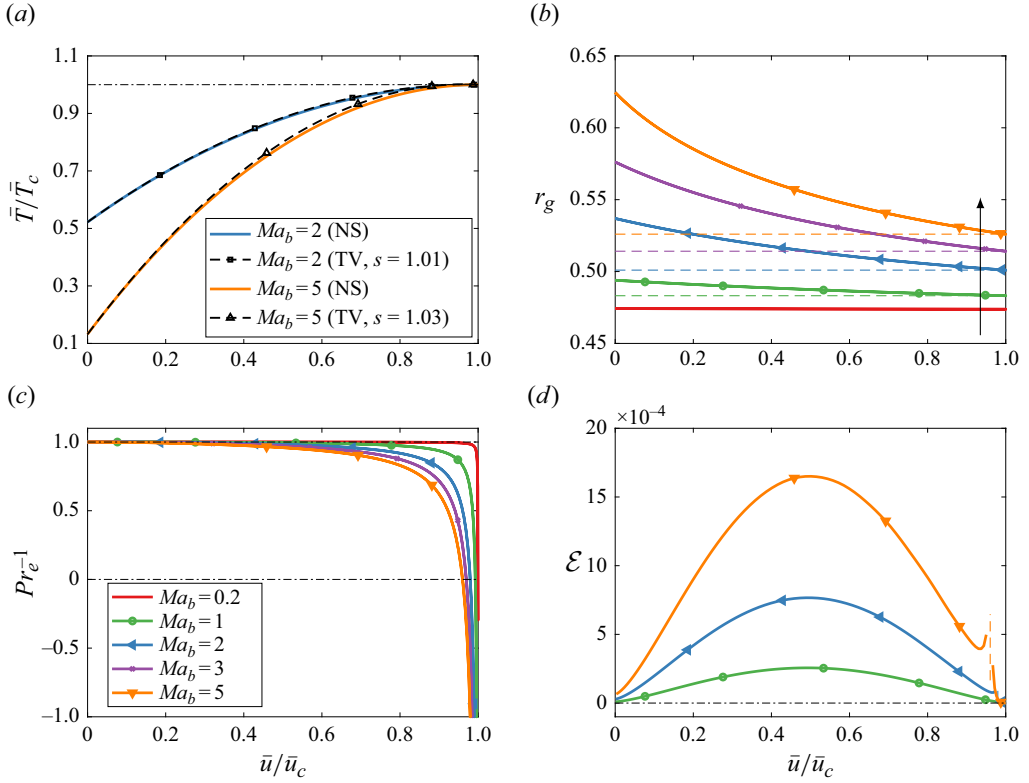
Figure 1. Laminar channel results: (*a*) temperature from NS equations and (1.1), (*b*) general recovery factor, (*c*) effective Prandtl number and (*d*) the sensitivity factor for flows at different Ma_b. The legends for panels (*b*)–(*d*) are the same.

The distributions of Pr_e^{-1} are plotted in figure 1(*c*) at $0 < Ma_b \leqslant 5$. Compared with r_g, Pr_e^{-1} is indeed less sensitive to Ma_b and is approximately unity at $\bar{u}/\bar{u}_c \lesssim 0.6$. In fact, its theoretical wall limit is just $Pr_{e,w} = 1$, obtained from (2.8). Further away from the wall, Pr_e^{-1} rapidly diminishes and can be negative. To better quantify the effects of Pr_e^{-1} variations, a sensitivity study on (2.4) is designed. Specifically, we compute the global variation of $\bar{T}$ when the Pr_e^{-1} at a specific y_0 is perturbed, i.e.

$$\mathcal{E}(y_0) = \frac{1}{\int_0^{\bar{u}_c} \bar{T} \, d\bar{u}} \int_0^{\bar{u}_c} \left| \frac{\partial \bar{T}(Pr_e^{-1}; \bar{u})}{\partial Pr_e^{-1}(y_0)} \right| d\bar{u}, \tag{2.9}$$

where $\bar{T}(Pr_e^{-1}; \bar{u})$ represents the solution of (2.4) on the $\bar{u}$ grid, under the outer boundary condition $\bar{T}|_{\bar{u}=\bar{u}_c} = \bar{T}_c$. The partial differentiation is computed after the numerical discretisation. The $\mathcal{E}$ in different cases are plotted in figure 1(*d*), where the spikes of $\mathcal{E}$ near the centreline are due to the singularity of Pr_e there ($Pr_e^{-1} = 0$). A general trend is that $\mathcal{E}$ peaks in the middle regime ($\bar{u} \approx 0.5\bar{u}_c$), and diminishes towards the wall and the centreline; meanwhile, $\mathcal{E}$ is amplified with the rise of Ma_b. These features are consistent with the trend in figure 1(*a*) that the TV relation slightly degrades in the middle region and with Ma_b increased.

Therefore, the success of the TV relation in figure 1(*a*) can be explained. On the one hand, the temperature is sensitive to the middle-regime Pr_e^{-1}, but Pr_e^{-1} is close to unity

Ma_b	0.01	0.5	1	2	3	4	5	6
s	0.976	0.980	0.987	1.007	1.021	1.029	1.034	1.037

Table 1. Reynolds analogy factor (2.5b) at different bulk Mach numbers for laminar channel flows.

there. On the other hand, Pr_e^{-1} deviates from unity further away towards the centreline, but $\bar{T}$ is already less sensitive to Pr_e^{-1}. More physical explanations on the above trends will be presented in § 2.3, through comparisons with the boundary layer cases. For modelling usage, we note that s varies mildly with Ma_b. As listed in table 1, s changes from 0.98 to 1.04 when Ma_b is ranged from 0.01 to 6. Thereby, the TV relation (1.1) with $s \approx 1$ is a highly accurate model for laminar channel flows.

2.3. *Laminar boundary layers*

The results for laminar boundary layers are rather different from § 2.2. The mean flow on a flat plate can be efficiently obtained by solving the self-similar equations (White 1974),

$$
\begin{cases}
C_1 \bar{u}_{\eta\eta} + \left(C_{1,\eta} + \dfrac{\Pi}{2} \right) \bar{u}_\eta = 0, \\
C_2 \bar{T}_{\eta\eta} + \left(C_{2,\eta} + c_p \dfrac{\Pi}{2} \right) \bar{T}_\eta + C_1 \bar{u}_\eta^2 = 0,
\end{cases}
\tag{2.10}
$$

where η is the transformed wall-normal coordinate, and $C_1 = \bar{\rho}\bar{\mu}/\bar{\rho}_e \bar{\mu}_e$, $C_2 = c_p C_1/Pr$ and $\Pi = \int \bar{u}/\bar{u}_e \, d\eta$. Equation (2.10) is independent of streamwise locations, and we consider cases at different free steam Mach numbers Ma_∞ (2–10) and $T_w/\bar{T}_r$ (0.1–1.6). The Chebyshev collocation point method with $N_y = 201$ is also adopted, which leads to grid-independent mean flow and GRA parameters.

The adiabatic wall cases ($T_w = \bar{T}_r$) are investigated first and the r_g at different Ma_∞ is shown in figure 2(*a*). It is found that r_g is not sensitive to Ma_∞ and exhibits a universal wall-normal distribution for adiabatic walls. Its theoretical wall limit, obtained from (2.10), is $r_{g,w} = Pr = 0.71$, which represents a balance between viscous terms and molecular heat flux (see Appendix A). Nevertheless, r_g is not a wall-normal constant, but keeps rising away from the wall due to stronger convection terms. The effects of wall cooling on r_g are displayed in figure 2(*b*) at $Ma_\infty = 6$. A clear trend is that as $T_w/\bar{T}_r$ drops, r_g exhibits weaker wall-normal variations, so the assumption of r_g constancy roughly holds only for severely cooled walls, which was shown by Mo & Gao (2024). Nevertheless, the above trend does not mean that the TV relation becomes more accurate for cooler walls, as will be shown later.

As learned from § 2.2, Pr_e is more significant than r_g in interpreting the shape of $\bar{T}$, so the Pr_e^{-1} at different Ma_∞ and $T_w/\bar{T}_r$ are plotted collectively in figure 2(*c*). A surprising observation is that the 20 curves (and also other Ma_∞ and $T_w/\bar{T}_r$ cases not displayed) almost collapse with each other, except for abrupt jumps near the temperature peaks in cold-wall cases. In other words, Pr_e^{-1} is nearly independent of Ma_∞ and T_w, beneficial for a robust modelling. The sensitivity examination of $\bar{T}$ on Pr_e^{-1} is also performed as in (2.9). As shown in figure 2(*d*), the outer region $\bar{T}$ is mostly affected by the deviation of Pr_e^{-1}, where Pr_e^{-1} systematically departs from unity. Consequently, different from the channel flows, the TV relation (1.1) for laminar boundary layers has systematic deviations
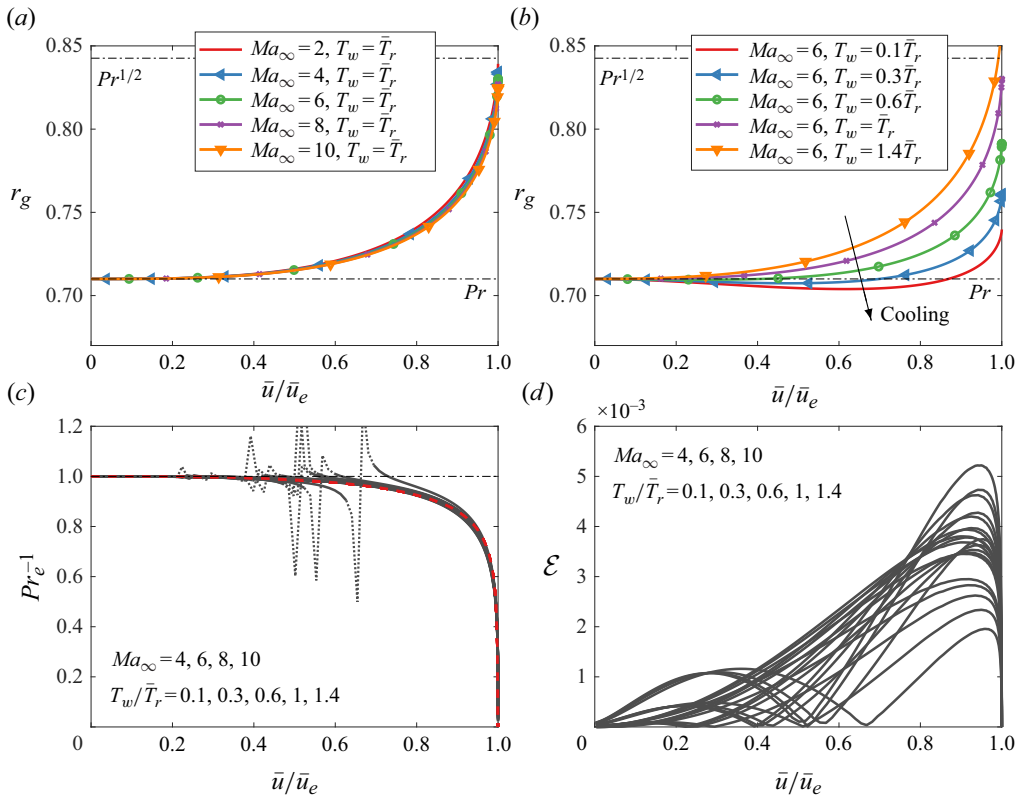
Figure 2. Laminar boundary layer results: general recovery factor for (*a*) adiabatic and (*b*) $Ma_\infty = 6$ isothermal cases, and (*c*) effective Prandtl number and (*d*) the sensitivity factor for 20 cases with different Ma_∞ and $T_w/\bar{T}_r$, as labelled. The jumps in panel (*c*) are plotted as dotted lines for conciseness, and the red dashed line denotes (2.13).

in the outer region, irrespective of Ma_∞ and T_w. This deviation is reflected by Mo & Gao (2024) (their figure 1*b*), and will be improved later.

Considering the collapse of Pr_e^{-1} among cases in terms of $\bar{u}/\bar{u}_e$, we seek for analytical relations from (2.10) for further interpretation. After eliminating the viscous parameters, an equation with separated variables is obtained (see Appendix A for derivations):

$$(1 - Pr)\frac{\Psi_{\bar{u}}}{\Psi_e - \Psi} = \frac{\bar{T}_{\bar{u}\bar{u}} - \bar{T}_{\bar{u}\bar{u},w}}{\bar{T}_{\bar{u}}} = \frac{\bar{Q}_{\bar{u}\bar{u}}}{\bar{T}_{\bar{u}}}, \qquad \Psi = \int_0^{\bar{u}} \Pi \, d\bar{u}, \qquad (2.11)$$

where the left-hand side relates to the velocity, and the right-hand sides correspond to the TV relation; the subscript $\bar{u}$ denotes partial derivatives. If $\bar{T}$ is a perfect quadratic function of $\bar{u}$, which is denoted as $\bar{T}_{qd}(\bar{u})$, then the second-order derivative $\bar{T}_{\bar{u}\bar{u}}$ is a constant and the right-hand sides should remain zero ($\bar{T}_{\bar{u}\bar{u}} = \bar{T}_{\bar{u}\bar{u},w}$). This is definitely invalid since the left-hand side monotonically increases from zero as $\bar{u}$ rises. In other words, a quadratic $\bar{T}(\bar{u})$ is not supported by the governing equation. Consequently, the non-zero right-hand side continuously contributes to the deviation of $\bar{T}$ from a quadratic function, though the accumulating error may be finally restricted by the enforced outer boundary condition $\bar{T}_e$. For clarity, we further define a residual temperature $\bar{Q} = \bar{T} - \bar{T}_{qd}$, then $\bar{Q} = 0$ means a perfect quadratic $\bar{T}(\bar{u})$ (see Appendix A for details). From (2.11), the second-order derivative of $\bar{Q}$ relates to Ψ, so $\bar{Q}_{\bar{u}\bar{u}}$ is non-zero except at the wall. However, substituting

1009 A39-8

$\bar{Q}$ into (2.3) and (2.4) results in expressions of Pr_e and r_g as

$$Pr_e^{-1} = 1 - \left(\frac{\bar{Q}}{\bar{u}^2}\right)_{\bar{u}} \frac{\bar{u}^2}{\bar{T}_{\bar{u}}}, \qquad r_g = Pr - 2c_p \frac{\bar{Q}}{\bar{u}^2}. \tag{2.12}$$

Therefore, the introduction of $\bar{Q}$ connects the deviation of $\bar{T}$ from $\bar{T}_{qd}$ with the departure of Pr_e from unity and of r_g from Pr.

Model improvement is required for laminar boundary layers considering the systematic deviation of Pr_e and thus (1.1). The robust distribution of Pr_e^{-1} in figure 2(c) can be modelled. For convenience of model usage, we provide a curve fitting

$$Pr_e^{-1} = 2 - [1 - (\bar{u}/\bar{u}_e)^3]^{-0.1}, \tag{2.13}$$

then (2.4) can be numerically solved. Another source of error besides Pr_e^{-1} is the estimation of s, required for the wall boundary condition. Unlike in § 2.2, s exhibits a moderate dependence on Ma_∞ and $T_w/\bar{T}_r$, as depicted in figure 3(a). Note that the s around $T_w \approx \bar{T}_r$ is not displayed because both the numerator and denominator tend to zero (see (2.5b)); the s there is also of little significance because $r_{g,e} \approx r$ when $T_w \approx \bar{T}_r$. The cold-wall boundary is more frequently encountered than the heated one in realistic high-speed applications (e.g. Bradshaw (1977); Chen *et al.* (2022b)). In the former case, s is generally 1.0–1.2, close to the turbulent counterparts. The temperature predictions using $Pr_e = 1$ (i.e. (1.1)) and the fitted Pr_e (2.13) are compared in figure 3(b), where $s = 1.14$ are used for both. As pointed out above, (1.1) systematically underestimates the temperature in the outer region ($\bar{u} \gtrsim 0.3\bar{u}_e$) at different Ma_∞ and $T_w/\bar{T}_r$. In comparison, solving (2.4) with (2.13) exhibits a notable improvement as expected, which attains a close agreement with the NS results.

To quantify the prediction accuracy of the TV relation, the relative error to the NS results,

$$\epsilon_T = \frac{\int_0^{\bar{u}_e} |\bar{T}_{NS} - \bar{T}_{TV}|\, d\bar{u}}{\int_0^{\bar{u}_e} \bar{T}_{NS}\, d\bar{u}}, \tag{2.14}$$

is computed. The errors from the two models are compared in figure 3(c) as a function of $T_w/\bar{T}_r$ for $Ma_\infty = 3$, 6, 10. Although r_g tends to be wall-normally invariant at low $T_w/\bar{T}_r$, the error of (1.1) for colder-wall cases is not lower but higher. At $Ma_\infty > 5$, ϵ_T is higher than 3 % for nearly all $T_w/\bar{T}_r$ conditions and its maximum reaches 7 %. In comparison, a notable reduction in ϵ_T is realised by using (2.13) for all the Ma_∞ and $T_w/\bar{T}_r$ shown. The improvement is most evident for cold-wall cases where ϵ_T are all less than 2 %, which has practical significance for high-speed realistic applications.

Finally, it is important to explain the different behaviours of r_g and Pr_e between channel and boundary layer cases. The channel flow is driven by the streamwise pressure gradient, which is a wall-normal constant, whereas for flat-plate boundary layers, the convection term acts as the driving force. In the latter case, the convection term is minor near the wall, so the rough balance between the viscous terms and molecular heat flux leads to $r_g \approx Pr$ in the near-wall region, as noted above. In contrast, the constant pressure gradient for channels disrupts the condition for constancy r_g ($\approx Pr$) near the wall, so r_g exhibits a converse trend that it varies more rapidly close to the wall than in the outer region. Another region worth discussing is that close to the boundary layer edge or the channel centreline, where the sensitivity of Pr_e largely differs between the two cases. For explanation, the numerator and denominator of Pr_e^{-1} in (2.8) are plotted in figure 4 for channel, and adiabatic and cold-wall boundary layers. The two curves in the channel case are nearly linear functions of $\bar{u}$ throughout the field. For the two boundary layer cases
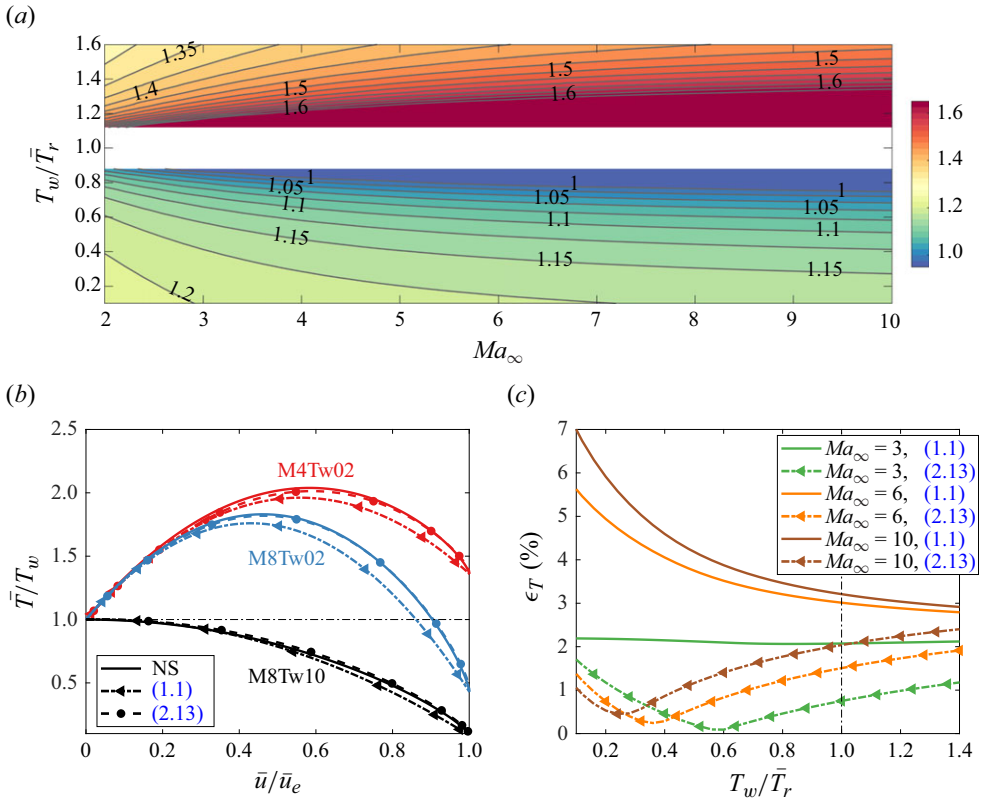
Figure 3. Laminar boundary layer results: (*a*) contours of the Reynolds analogy factor at different Ma_∞ and $T_w/\bar{T}_r$; (*b*) temperature from NS equations, (1.1) and (2.13) for three cases, and (*c*) the prediction error of $\bar{T}$ at different Ma_∞ and $T_w/\bar{T}_r$. The notation M4Tw02 in panel (*b*) denotes $Ma_\infty = 4$, $T_w = 0.2\bar{T}_r$ and the same for the others.

(figures 4*b* and 4*c*), however, $\partial\bar{T}/\partial\bar{u}$ declines dramatically near the edge ($\bar{u} \gtrsim 0.8\bar{u}_e$), leading to the uncertainty and sensitivity of Pr_e. The sudden mismatch of the two curves near the edge is due to the thickness difference between the momentum and thermal boundary layers, i.e. $\delta_u \neq \delta_T$, since $Pr \neq 1$. Therefore, the TV relation is difficult to follow in the transition region between δ_u and δ_T. This transition region does not exist in the channel case because the thicknesses of the momentum and thermal layers are forced to be the same, equal to h. In short, two primary factors responsible for the differences between channel and boundary layers are the spatial distribution of the driving force, and the thicknesses of the momentum and thermal boundary layers.

2.4. *Turbulent boundary layers*

In the following, turbulent cases are dealt with using wide elaborated DNS data. For turbulent boundary layers, 17 DNS cases from five different sources are employed with Ma_∞ from 2 to 14 under cold, adiabatic and heated walls ($T_w/\bar{T}_r = 0.18 - 1.9$). The specific parameters and data sources of these cases are listed in table 2.

The mean flow $\bar{u}$ and $\bar{T}$ are employed to compute Pr_e and r_g. The adiabatic and heated wall cases are considered first, whose Pr_e^{-1} distributions are plotted in figure 5(*a*). Here, Pr_e^{-1} is indeed around unity in most regions, which explains the wide success of (1.1) for these cases. Meanwhile, Pr_e^{-1} declines markedly near the boundary layer edge
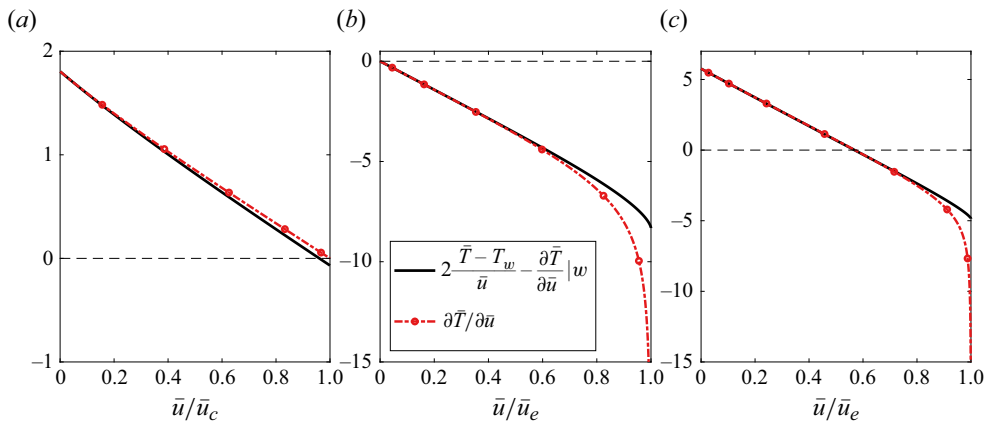
1009 A39-10

Figure 4. Numerator and denominator of Pr_e^{-1} in (2.8) for (a) laminar channel case $Ma_b = 5$, and laminar boundary layer cases (b) $Ma_\infty = 5$, $T_w = \bar{T}_r$ and (c) $Ma_\infty = 5$, $T_w = 0.1\bar{T}_r$. All the curves are normalised by $\bar{T}_c/\bar{u}_c$ or $\bar{T}_e/\bar{u}_e$, accordingly.

No.	Source	Notation	Ma_∞	$T_w/\bar{T}_r$	Θ	Re_θ	Re_τ
1	PB	M2Tw10R39	2.0	1.0	1.0	6040	1113
2	ZDC	M2p5Tw10R17	2.50	1.0	1.0	2835	510
3	PB	M3Tw10R18	3.0	1.0	1.0	4340	502
4	PB	M4Tw10R21	4.0	1.0	1.0	5910	505
5	ZWLSL	M6Tw10R32	6.0	1.0	1.0	20460	622
6	ZWLSL	M8Tw10R38	8.0	1.0	1.0	35710	623
7	VBL	M2Tw19R3	2.28	1.9	2.84	870	100
8	VBL	M5Tw19R7	5.0	1.9	2.06	3900	176
9	VBL	M2Tw05R13	2.28	0.5	−0.04	1250	512
10	ZWLSL	M4Tw05R20	4.0	0.5	0.32	3328	675
11	VBL	M5Tw08R23	5.0	0.8	0.74	6980	685
12	ZDC	M6Tw025R11	5.84	0.25	0.13	2121	450
13	ZDC	M6Tw076R17	5.86	0.76	0.71	9455	453
14	CSPB	M6Tw076R84	5.86	0.76	0.72	29349	1947
15	ZWLSL	M8Tw025R20	8.0	0.25	0.18	6465	615
16	ZDC	M8Tw048R20	7.87	0.48	0.43	9714	480
17	ZDC	M14Tw018R24	13.64	0.18	0.16	14408	646

Table 2. Parameters of the turbulent boundary layer DNS datasets, where Re_τ and Re_θ are the friction and momentum-thickness-based Reynolds numbers. The abbreviations for data sources are: PB for Pirozzoli & Bernardini (2011, 2013); ZDC for Zhang *et al.* (2018); VBL for Volpiani *et al.* (2018, 2020); ZWLSL for Zhang *et al.* (2022); and CSPB for Cogo *et al.* (2022). The notation expresses Ma_∞, $T_w/\bar{T}_r$ and $Re_{\delta_2} = \rho_\infty u_\infty \delta_{99}/\bar{\mu}_w$ (divided by 100) with ρ the density and δ_{99} the nominal thickness.

($\bar{u} \gtrsim 0.9\bar{u}_e$) for all cases, in line with the laminar case in figure 2(c). This is not unexpected because the flow has become episodic and intermittent near the edge (Zhang *et al.* 2014), and the momentum and thermal boundary layers differ in thicknesses as $Pr \neq 1$ (see § 2.3). The cold wall cases are considered separately in figure 5(b) because there are temperature peaks inside the boundary layer, around which Pr_e^{-1} becomes singular due to the diminishing $\partial\bar{T}/\partial\bar{u}$. The Pr_e^{-1} varies dramatically around the temperature peak, but it becomes close to unity again further away from the wall, the same as in figure 5(a). The sensitivity examination is similarly conducted as for laminar flows to study the influence of
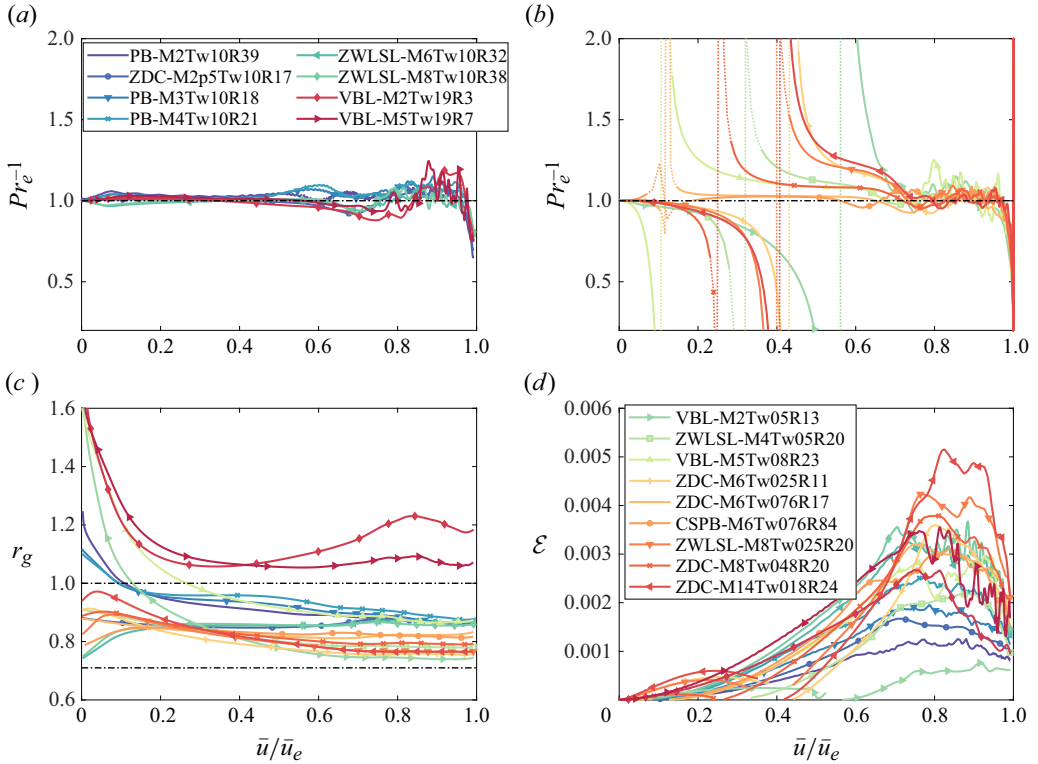
Figure 5. Turbulent boundary layer results: effective Prandtl number for (*a*) adiabatic and heated-wall cases and (*b*) cold-wall cases, and (*c*) general recovery factor and (*d*) the sensitivity factor for all cases. The legends (see notation in table 2) are the same for all panels, separately shown in the two boxes.

Pr_e^{-1} variations on $\bar{T}$. As shown in figure 5(*d*), $\mathcal{E}$ is mostly amplified at $\bar{u} \gtrsim 0.7\bar{u}_e$, where Pr_e^{-1} is close to unity. Also, the dramatic variation of Pr_e^{-1} near the temperature peak for cold-wall cases limitedly influences the accuracy of the TV quadratic relation owing to the relatively low $\mathcal{E}$. The above two facts support the wide accuracy of (1.1) for turbulent boundary layers.

In addition to Pr_e^{-1}, the r_g profiles of all cases are collectively displayed in figure 5(*c*). We note that the near-wall r_g (at $\bar{u} \lesssim 0.1\bar{u}_e$) can be highly sensitive to $\partial \bar{T}/\partial \bar{u}|_w$ and thus the post-processing discretisation schemes, because both the numerator and denominator in (2.2*b*) and their first-order derivatives are zero at the wall. We use the Chebyshev collocation point method to compute these derivatives and ensure that the results are grid independent by increasing N_y up to 401. Using other schemes may lead to different near-wall r_g, but the primary conclusions remain unaltered. For all the cases, r_g tends to be invariant at $\bar{u} \gtrsim 0.5\bar{u}_e$, but the near-wall r_g rapidly changes, not following constancy.

The velocity and temperature transformations can provide insights into the near-wall behaviour of r_g. The major difference between the temperature transformation and the TV relation is that, the former is derived from the energy equation (Patel, Boersma & Pecnik 2017; Chen *et al.* 2022*a*), while the latter is built upon the analogy between momentum and energy equations. Therefore, the three relations (two transformations and the TV relation) firmly connect with each other. We first consider the TL velocity transformation of Trettel & Larsson (2016) and the semi-local temperature transformation of Chen *et al.* (2022*a*). In the viscous sublayer, these two transformations can reproduce the incompressible scalings

of velocity and temperature, under the semi-local units. The transformed velocity and temperature ($\bar{\theta} = \bar{T} - T_w$) follow

$$\bar{u}_{TL}^+(y^*) = \int_0^{y^*} \bar{\mu}^+ \frac{\partial \bar{u}^+}{\partial y^+} \mathrm{d}y^* \approx y^*, \tag{2.15a}$$

$$\bar{\theta}_{SL}^+(y^*) = \int_0^{y^*} \frac{\frac{y^+}{y^*}\sqrt{\bar{\rho}^+}\frac{\partial \bar{\theta}^+}{\partial y^+}}{1 - \frac{\bar{u}\bar{\tau}_w}{\bar{q}_w}} \mathrm{d}y^* \approx Pr\, y^*, \tag{2.15b}$$

where $y^* = y^+ \bar{\rho}^{+1/2}/\bar{\mu}^+$ is the semi-local coordinate; $\bar{u}^+$, $\bar{\rho}^+$, y^+, $\bar{\mu}^+$ and $\bar{\theta}^+$ are normalised by the wall viscous units $u_\tau = (\bar{\tau}_w/\bar{\rho}_w)^{1/2}$, $\bar{\rho}_w$, $\bar{\mu}_w/(\bar{\rho}_w u_\tau)$, $\bar{\mu}_w$ and $T_\tau = \bar{q}_w/(\bar{\rho}_w c_p u_\tau)$, respectively. Note that (2.15b) is the re-derived version by Cheng & Fu (2024a) for channels and boundary layers, essentially the same as the original version for Couette flows. Also, for adiabatic walls with $\bar{q}_w \approx 0$ and $T_\tau \approx 0$, (2.15b) can still be defined by multiplying the numerator and denominator by a factor $\bar{q}_w$ (Chen *et al.* 2022a). The combination of (2.15a) and (2.15b) yields a simple TV relation (derivation in Appendix A),

$$\frac{\partial \bar{\theta}^+}{\partial \bar{u}^+} = Pr\left(1 - \frac{u_\tau^2}{c_p T_\tau}\bar{u}^+\right) \quad \text{or} \quad \frac{\partial \bar{T}}{\partial \bar{u}} = \frac{Pr}{c_p}\left(\frac{\bar{q}_w}{\bar{\tau}_w} - \bar{u}\right) = \frac{\partial \bar{T}}{\partial \bar{u}}|_w - \frac{Pr}{c_p}\bar{u}. \tag{2.16}$$

Therefore, (2.16) by itself suggests a quadratic relation between $\bar{T}$ and $\bar{u}$ near the wall. An analytical relation is further obtained by substituting (2.16) into (2.2 a) that $r_g = Pr$ in the viscous sublayer, irrespective of wall thermal boundary conditions (see Appendix A). This relation results directly from the balance between viscous terms and molecular heat flux, the same as the laminar case in § 2.3. Nevertheless, the near-wall $r_g \approx Pr$ is not in line with figure 5(c), so we conclude that the accuracy of these transformations (2.15) is only guaranteed integrally. Their point-by-point derivatives may not be accurate enough. Similar analyses for the buffer and logarithmic layers can be performed using the GFM velocity transformation of Griffin *et al.* (2021b), and the temperature transformation of Cheng & Fu (2024a), which will be used in § 3 to implement a new temperature wall model.

2.5. *Turbulent channel flows*

The turbulent channel flows are studied using 12 DNS cases with $Ma_b \leqslant 4$, whose parameters and data sources are detailed in table 3. As shown in figure 6(a), the r_g of these cases generally experiences a decreasing trend away from the wall, and the Reynolds number effect on r_g is weak. The near-wall r_g also does not follow the constancy deduced from (2.16), i.e. $r_g \approx Pr$, like the boundary layer cases, though the two transformations in (2.15) are generally applicable to the channel cases in the viscous sublayer. Moreover, the centrelines r_g ($r_{g,c}$) all fall within 0.62 ± 0.01 for these cases, which is also reflected from the weakly varied Θ in table 3 (see (2.5a)). Nonetheless, substituting the $\bar{T}_c$ scaling derived by Song *et al.* (2022) into (2.5a) suggests a weak dependence of $r_{g,c}$ on $\bar{u}_c/\bar{u}_b$, as

$$r_{g,c} = Pr\left[sr - 1.034(1 - sPr)\bar{u}_b/\bar{u}_c\right]. \tag{2.17}$$

As shown in figure 6(b), Pr_e^{-1} systematically deviates from unity in the middle regime $0.2 \lesssim \bar{u}/\bar{u}_c \lesssim 0.7$, different from the boundary layer cases in § 2.4. Meanwhile, there is a pronounced sensitivity of $\bar{T}$ on Pr_e^{-1} in that region, as seen from figure 6(d), and the sensitivity ($\mathcal{E}$) rapidly grows with the rise of Ma_b. Consequently, the quadratic relation

No.	Source	Notation	Ma_b	Re_τ	$\bar{u}_c/\bar{u}_b$	$\bar{T}_c/T_w$	Θ
1	TL	M07R4	0.7	440	1.15	1.08	−0.72
2	TL	M07R7	0.7	650	1.14	1.08	−0.73
3	YH	M08R9	0.8	910	1.14	1.11	−0.73
4	YH	M08R17	0.8	1690	1.12	1.11	−0.76
5	YH	M15R10	1.5	1030	1.14	1.39	−0.74
6	CF	M15R12	1.5	1160	1.14	1.39	−0.74
7	YH	M15R19	1.5	1910	1.13	1.39	−0.77
8	TL	M17R7	1.7	660	1.15	1.48	−0.72
9	TL	M17R10	1.7	970	1.15	1.48	−0.72
10	TL	M30R12	3.0	1230	1.15	2.49	−0.72
11	TL	M30R19	3.0	1880	1.15	2.49	−0.72
12	TL	M40R10	3.9	1020	1.17	3.64	−0.72

Table 3. Parameters of the turbulent channel DNS datasets. The abbreviations for data sources are: TL for Trettel & Larsson (2016); YH for Yao & Hussain (2020); and CF for Cheng & Fu (2022). The notation expresses Ma_b and Re_τ (divided by 100). Note that TL uses the power viscous law instead of sutherland's law.
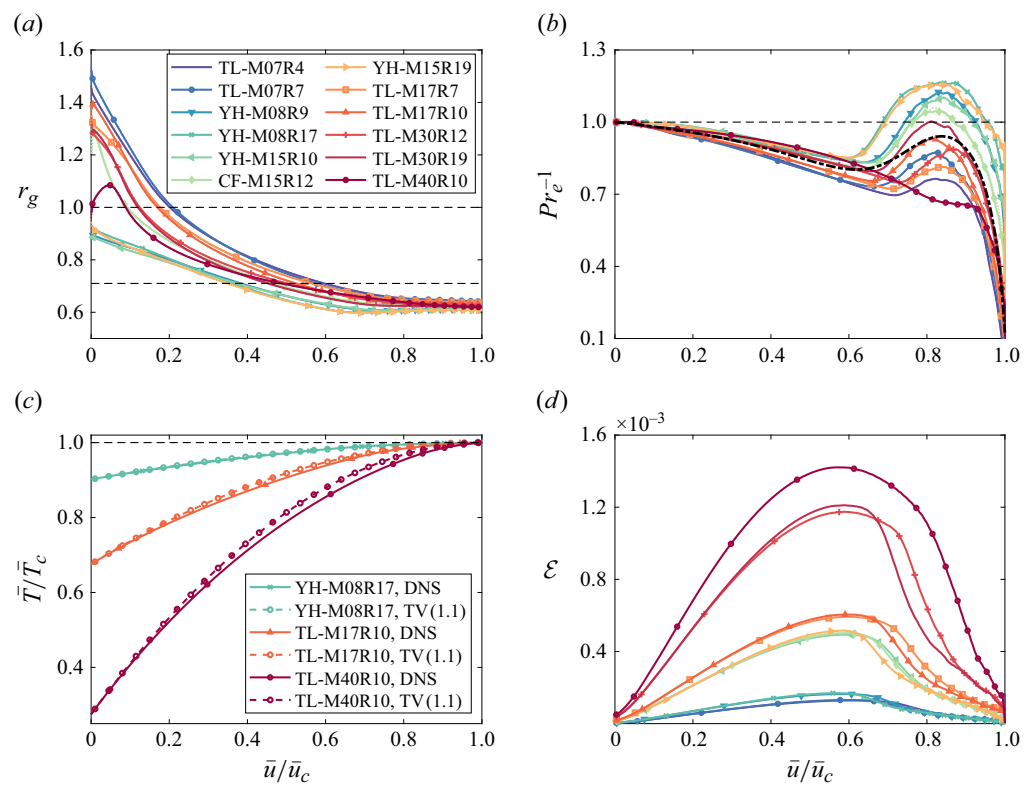

Figure 6. Turbulent channel results: (*a*) general recovery factor; (*b*) effective Prandtl number; (*c*) mean temperature from DNS and (1.1); and (*d*) the sensitivity factor for different cases. The legends (see notation in table 3) are the same for panel (*a*,*b*,*d*). The black dashed line in panel (*b*) is a fitted curve detailed in Appendix B.
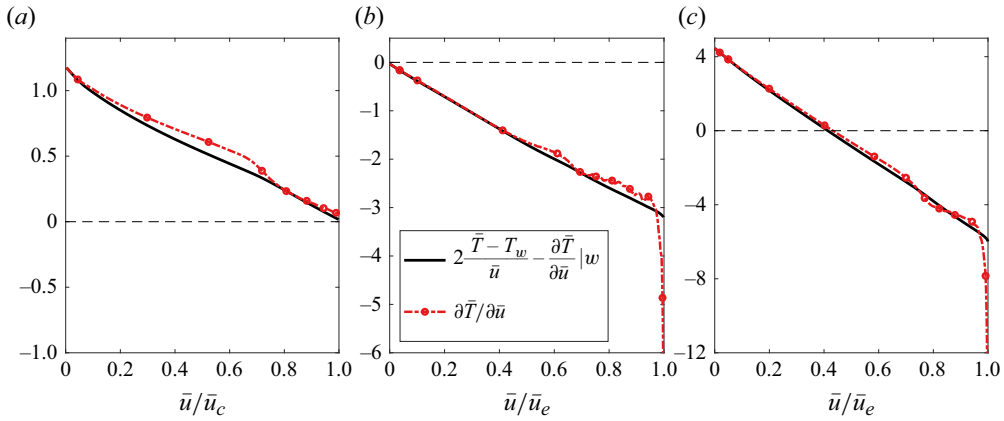
Figure 7. Numerator and denominator of Pr_e^{-1} in (2.8) for turbulent (*a*) channel case TL-M30R19, and boundary layer cases (*b*) adiabatic PB-M3Tw10R14 and (*c*) cold-wall ZDC-M6Tw025R11. All the curves are normalised by $\bar{T}_c/\bar{u}_c$ or $\bar{T}_e/\bar{u}_e$, accordingly.

(1.1) has a modest deviation (overprediction) in the middle regime, especially for high-Ma_b cases, which is clearly demonstrated in figure 6(*c*). The fact that (1.1) performs better for turbulent boundary layers than turbulent channel flows is reasonable, because the constant pressure gradient term in the channel momentum equation hinders the GRA between momentum and energy equations. For modelling usage, a curve fitting of Pr_e^{-1} in figure 6(*b*) can be made, similar to the implementation for (2.13) and figure 3, to improve the accuracy of the TV relation for turbulent channel flows. A sample is provided in Appendix B.

Considering the different behaviours of Pr_e between laminar and turbulent cases, the numerator and denominator of Pr_e^{-1} in (2.8) for three turbulent cases are plotted in figure 7, in a similar style to figure 4. For turbulent boundary layers, the major difference from the laminar counterpart is that $\partial\bar{T}/\partial\bar{u}$ in figures 4(*b*) and 4(*c*) follow more closely the denominator, until $\bar{u} \approx 0.97\bar{u}_e$, so the TV relation is more accurate than the laminar boundary layers. This enhanced TV connection in the outer region in turbulent cases can be attributed to the intense wall-normal eddy transport of momentum and energy, and the strong TV fluctuation coupling of very large scale motions (Jiménez *et al.* 2010; Pirozzoli & Bernardini 2011; Cheng & Fu 2023, 2024*b*).

3. A new temperature wall model

As introduced in § 1, (1.1) has been employed as a temperature wall model for the inner layer to increase the prediction accuracy of laminar and turbulent mean flows. Nevertheless, (1.1) is dependent on boundary-layer-edge quantities $\bar{u}_e$ and $\bar{T}_e$, so this wall model is less applicable to complicated flow configurations. In this section, we discuss how to remove the dependence of the temperature wall model on $\bar{u}_e$ and $\bar{T}_e$ for turbulent boundary layers. In fact, Mo & Gao (2024) has proposed one solution for laminar flows to remove the usage of $\bar{u}_e$ and $\bar{T}_e$, but their strategy cannot be directly extended to turbulent cases. The main difficulties and possible solutions are presented in the following.

The $Pr_e \approx 1$ case is considered first. The introduction of a temperature wall model is in the same spirit as the velocity counterpart, where the inner layer and outer layer of the velocity are treated separately for improved scalings of near-wall eddy viscosity (Griffin *et al.* 2023; Hasan *et al.* 2024). Within the frameworks of RANS and WMLES, (1.1) can
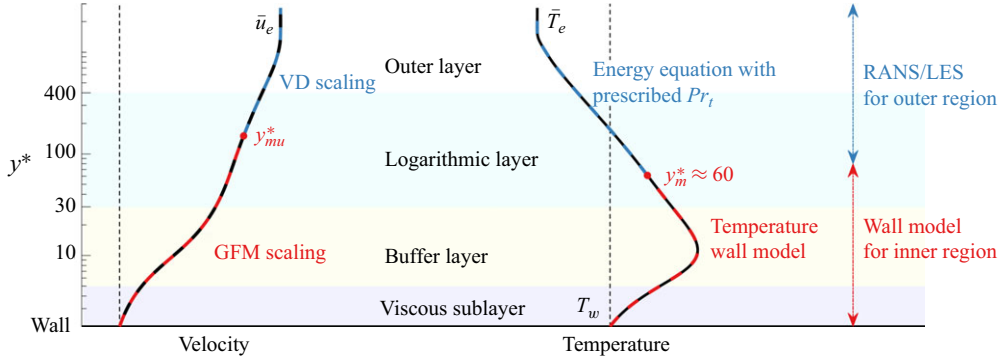
Figure 8. Illustration of the RANS/WMLES frameworks using velocity transformations and temperature wall models in the inner layer for improved near-wall scalings, following Griffin *et al.* (2023) and Chen *et al.* (2024). y_{mu}^* and y_m^* are the matching points of streamwise velocity (eddy viscosity) and temperature, respectively.

be employed as a temperature wall model in the inner layer $y < y_m$ with y_m the matching point, as illustrated in figure 8. The outer region $y > y_m$ is still solved from the RANS or LES equations (Griffin *et al.* 2023; Chen *et al.* 2024). This modelling strategy does not introduce additional empirical functions and can effectively improve the temperature prediction, especially for cold-wall cases, compared with the conventional method which solves the RANS equation in the inner layer with prescribed turbulent Prandtl number Pr_t. The reason is that the inner-layer $\bar{T}$ is sensitive to local Pr_t, and Pr_t can dramatically vary with y and be singular near the wall in boundary layers, especially for cold-wall cases (Subbareddy & Candler 2012; Chen *et al.* 2024). Also, the near-wall Pr_t can change considerably from case to case, so a universal and simple model of Pr_t (or the eddy diffusivity) for boundary layers is not currently available.

Using the field samples at y_m, i.e. $\bar{u}_m$ and $\bar{T}_m$, as the outer boundary condition, the solution of (2.4) reads

$$\bar{T} = T_w + \frac{\partial \bar{T}}{\partial \bar{u}}|_w \bar{u}\left(1 - \frac{\bar{u}}{\bar{u}_m}\right) + (\bar{T}_m - T_w)\frac{\bar{u}^2}{\bar{u}_m^2}, \tag{3.1}$$

so the only unknown is $(\partial \bar{T}/\partial \bar{u})_w$. Note that for adiabatic walls, $(\partial \bar{T}/\partial \bar{u})_w$ is zero and T_w is unknown. This case can be converted into an approximately isothermal-wall case with $T_w = \bar{T}_r$, as adopted by, e.g. Pirozzoli & Bernardini (2011) in their DNS. From the GRA in § 2.1, $(\partial \bar{T}/\partial \bar{u})_w$ robustly relates to the boundary-layer-edge quantities,

$$\frac{\partial \bar{T}}{\partial \bar{u}}|_w = \frac{Pr}{c_p}\frac{\bar{q}_w}{\bar{\tau}_w} = \frac{\bar{u}_e r_{g,e}}{2c_p} + \frac{\bar{T}_e - T_w}{\bar{u}_e} = \frac{s\,Pr(\bar{T}_r - T_w)}{\bar{u}_e}. \tag{3.2}$$

Equation (3.2) demonstrates where $\bar{u}_e$ and $\bar{T}_e$ are involved in the temperature wall model. This TV wall model using (3.1) and (3.2) is adopted by Griffin *et al.* (2023) and Chen *et al.* (2024). For laminar flows, Mo & Gao (2024) propose that $\bar{u}_e$ and $\bar{T}_e$ can be excluded by designing the wall model as a post-processing method, or an inverse problem. This strategy is built upon the fact that even though the near-wall mesh is coarse, the laminar mean flow off the wall can be accurately attained using the NS equation, then the temperature wall model can be used inversely to improve the estimation of the wall temperature gradient. Specifically, $(\partial \bar{T}/\partial \bar{u})_w$ can be obtained inversely from (3.1) using a coarse-mesh $\bar{T}$ (three grid samples to determine the quadratic function), then (3.2) enables accurate recovery of τ_w and q_w, combined with velocity transformations. Furthermore, since this laminar wall

1009 A39-16

model excludes the use of the edge quantities, Mo & Gao (2024) showed that it can be directly applied to laminar curved-wall cases. For turbulent flows, however, this strategy of an inverse problem is not applicable due to the inclosure or inaccuracy of near-wall RANS equations. In other words, $(\partial \bar{T}/\partial \bar{u})_w$ needs to be determined prior to $\bar{T}$, so the temperature wall model should be coupled with the governing equation during the iteration of the flow field.

Next, we search for alternatives to (3.2) in determining $(\partial \bar{T}/\partial \bar{u})_w$. A straightforward thought is to establish relations between $(\partial \bar{T}/\partial \bar{u})_w$ and $\bar{u}_m$, $\bar{T}_m$, in a similar form to (3.2). For example, a simple idea is to directly replace ϕ_e (ϕ denotes variables) in (3.2) with ϕ_m. Unfortunately, the resulting $r_{g,m}$ and s_m vary markedly with y_m, as inferred from their wall-normal variations in § 2, which obstructs robust modellings. We provide another solution by incorporating the temperature transformation in the wall model. Since the temperature transformation is derived from the energy equation, it provides extra constraints to the TV relation, hence providing a closure condition. The temperature transformation of Cheng & Fu (2024a) is employed, which was shown to perform better in boundary layer cases than other transformations. The transformed temperature for the inner layer takes the form

$$\bar{\theta}_S^+(y^*) = \int_0^{y^*} \Phi_S^+ \, \mathrm{d}y^* = \int_0^{y^*} \frac{\sqrt{\bar{\rho}^+} \frac{\partial \bar{\theta}^+}{\partial y^*}}{1 - \frac{\bar{u}\bar{\tau}_w}{\bar{q}_w}} \mathrm{d}y^*, \tag{3.3}$$

which does not involve boundary-layer-edge values; here, Φ_S^+ is the transformation kernel. It is worth emphasising that the transformations (2.15b) and (3.3) are derived from the original unmodelled turbulent energy equation, not from the modelled one involving Pr_t models.

Ideally, $\bar{\theta}_S^+(y^*)$ should collapse with the incompressible counterpart with heat transfer $\bar{\theta}_{inc}^+(y^+)$ (Kader 1981; Alcántara-Ávila *et al.* 2021). It is important to remark that if in that case, there is no need to compute $(\partial \bar{T}/\partial \bar{u})_w$ and use the TV relation as the wall model, because the velocity and temperature transformations already constitute a closed system to compute the inner-layer $\bar{u}$ and $\bar{T}$. However, unfortunately, current temperature transformations are not as accurate as the velocity counterparts, especially for cold-wall cases. A critical challenge is the non-monotonicity of $\bar{T}(y)$ for cold-wall cases. Based on the relation of local heat transfer (e.g. Bradshaw, Huang & Launder (1995)), $\bar{q} \approx \bar{q}_w - \bar{u}\bar{\tau}_w$, the denominator in (3.3) (and also (2.15b)) can be zero near the temperature peak $y_{\bar{T}_y = 0}$ where $\bar{q} \approx 0$, then $\bar{\theta}_S^+$ is ill-defined or singular. Consequently, the inner-layer $\bar{T}$ up to the logarithmic region cannot be constructed as a whole.

A positive result from Cheng & Fu (2024a) is that the two parts of $\bar{\theta}_S^+$ below and above the singular point can be constructed separately. For example, the latter part is formulated as

$$\bar{\theta}_S^+(y^*) = \bar{\theta}_{ref}^+(y_{\bar{T}_y = 0}^{*(+)}) + \int_{y_{\bar{T}_y = 0}^{*(+)}}^{y^*} \Phi_S^+ \, \mathrm{d}y^* \quad \text{for } y^* > y_{\bar{T}_y = 0}^{*(+)}, \tag{3.4}$$

where $y_{\bar{T}_y = 0}^{*(+)}$ is a point above $y_{\bar{T}_y = 0}^*$ and $\bar{\theta}_{ref}^+$ is a reference value discussed later. For all the datasets in table 2, $y_{\bar{T}_y = 0}^*$ falls within or below the buffer layer, so (3.4) can be constructed for the logarithmic region. Cheng & Fu (2024a) showed that (see their figure 14) the two parts of $\bar{\theta}_S^+(y^*)$ below and above the singular point can generally match with $\bar{\theta}_{inc}^+(y^+)$, respectively. In other words, the match between $\bar{\theta}_S^+$ and $\bar{\theta}_{inc}^+$ are piecewise, in the

two regions away from $y^*_{\bar{T}_y = 0}$. Particularly, $\bar{\theta}^+_S(y^*)$ in (3.4) can follow the incompressible logarithmic scaling of temperature, where their reference point is at $y^* = 50$. Note that very recently, Gibis *et al.* (2024) presented a comprehensive summary of $y^*_{\bar{T}_y = 0}$ for turbulent boundary layers. They revealed its dependence on Θ and Re_τ, and showed that the temperature peak can move higher into the logarithmic region for strongly cooled walls ($\Theta < 0$) and high-Re_τ ($\gtrsim 10^4$) regions, so then $y^{*(+)}_{\bar{T}_y = 0}$ needs to be larger accordingly. As a result of the match with the incompressible scaling of temperature, a combined strategy can be designed that we first compute $(\partial \bar{T}/\partial \bar{u})_w$ from a selected point of (3.3), and then use (3.1) to construct the inner-layer $\bar{T}$. This new implementation excludes the usage of boundary-layer-edge quantities. If $Pr_e \approx 1$ is not followed, the above framework is also feasible, because (2.4) can be directly solved using a prescribed modelled Pr_e and the $(\partial \bar{T}/\partial \bar{u})_w$ from temperature transformations.

The specific expressions are presented below. Since the matching point of a wall model is usually in the logarithmic layer (see figure 8), we consider the region above the singular point of $\bar{\theta}^+_S$, i.e. (3.4). Considering the piecewise match between $\bar{\theta}^+_S$ and $\bar{\theta}^+_{inc}$, the transformation is rewritten in its derivative form, based on (3.3) or (3.4), as

$$
\frac{d\bar{\theta}^+_{inc}}{dy^+} \approx \frac{d\bar{\theta}^+_S}{dy^*} = \Phi^+_S = \frac{\sqrt{\bar{\rho}^+} \frac{\partial \bar{u}^+}{\partial y^*} \frac{\partial \bar{T}}{\partial \bar{u}}}{\frac{1}{Pr} \frac{\partial \bar{T}}{\partial \bar{u}}|_w - \frac{\bar{u}}{c_p}} \quad \text{for } y^* > y^{*(+)}_{\bar{T}_y = 0},
$$

$$
\text{where} \quad \frac{\partial \bar{T}}{\partial \bar{u}} = \frac{\partial \bar{T}}{\partial \bar{u}}|_w \left(1 - \frac{2\bar{u}}{\bar{u}_s}\right) + (\bar{T}_s - T_w)\frac{2\bar{u}}{\bar{u}_s^2}.
$$

(3.5)

Here, the expression of $\partial \bar{T}/\partial \bar{u}$ originates from (3.1), except for using another set of field samples $\bar{u}_s$, $\bar{T}_s$ at y_s. The point y_s just provides a reference to the TV relation, and for practical use, it can be any point inside or outside (then $\phi_s = \phi_e$) the boundary layer, provided $y_s \geqslant y_m$. Compared with (3.4), the reference value $\bar{\theta}^+_{ref}$ is eliminated in (3.5) due to the derivative operation, hence not required to be specified. Afterwards, $(\partial \bar{T}/\partial \bar{u})_w$ can be obtained inversely from (3.5) at a single point, using local variables, reference values at y_s and $\bar{\theta}^+_{inc}$. The incompressible reference $\bar{\theta}^+_{inc}(y^+)$ uses the DNS data of Alcántara-Ávila *et al.* (2021), with Re_τ up to 5000. The point-by-point derivatives can be sensitive to local perturbations, so (3.5) is also rewritten into an integral manner to improve robustness, as

$$
\bar{\theta}^+_{inc}|^{y^+}_{20} \approx \bar{\theta}^+_S|^{y^*}_{20} = \int_{20}^{y^*} \frac{\sqrt{\bar{\rho}^+} \frac{\partial \bar{u}^+}{\partial y^*} \frac{\partial \bar{T}}{\partial \bar{u}}}{\frac{1}{Pr} \frac{\partial \bar{T}}{\partial \bar{u}}|_w - \frac{\bar{u}}{c_p}} dy^*.
$$

(3.6)

Here, the lower limit of integration is simply set to 20 in the buffer layer, considering the relatively low $y^*_{\bar{T}_y = 0}$ (<20) under the present Θ and Re_τ ranges in table 2. In the following, we first examine *a priori* the accuracy of $(\partial \bar{T}/\partial \bar{u})_w$ from (3.5) and (3.6) using the DNS data. Second, we implement the new temperature wall model in RANS simulations to test *a posteriori* the temperature prediction.

Chen *et al.* (2024) found that the temperature wall model is most effective for highly cooled-wall cases in terms of improving the temperature prediction. Therefore, we also focus on such wall conditions and follow Gibis *et al.* (2024) to use Θ instead of $T_w/\bar{T}_r$ to classify different wall-cooling regimes. For the cases in table 2, those with $\Theta < 0.2$ and with $0.2 \leqslant \Theta < 0.5$ are termed severe and modest cooling cases, respectively. We plot in figure 9 the $(\partial \bar{T}/\partial \bar{u})_w$ computed from (3.5) and (3.6), respectively, for the six
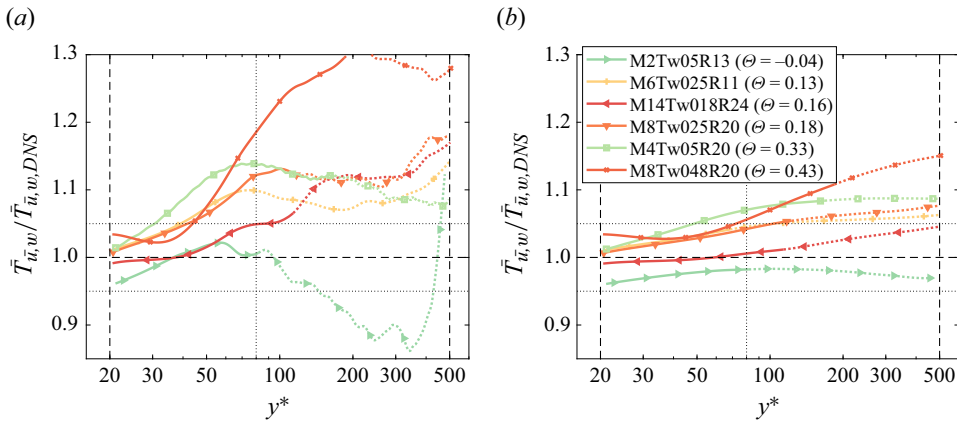
Figure 9. Ratios of $(\partial \bar{T}/\partial \bar{u})_w$ (*a*) from (3.5) and (*b*) from (3.6) to the DNS data for six severe or modest cooling turbulent boundary layer cases, sorted by Θ. The curves at $y/\delta_{99} > 0.2$ are plotted by dotted lines.

severe and modest cooling cases. For convenience of inter-case comparisons, the results are shown in ratios to $(\partial \bar{T}/\partial \bar{u})_w$ from the DNS data. Since the temperature transformation is not expected to work above the logarithmic region, the curves at $y/\delta_{99} > 0.2$ are plotted as dotted lines. As shown in figure 9(*a*), the accuracy of (3.5) varies dramatically with y^*. The maximum relative error reaches 30 % for case ZDC-M8Tw048R20. After using the integral version (3.6), the prediction of $(\partial \bar{T}/\partial \bar{u})_w$ becomes much more robust, and the relative errors to DNS are all less than 5 % within $y^* < 80$ for the severe cooling cases. Therefore, incorporating the temperature transformation is a viable path to estimate $(\partial \bar{T}/\partial \bar{u})_w$ without using the boundary-layer-edge values. It is worth mentioning that the accuracy of (3.6) may be further improved by adding to (3.3) the functions related to high-order fluctuation terms (Cheng & Fu 2024*a*). Nevertheless, the simplest form is adopt here for convenience of modelling usage. Equations (3.1) and (3.6) constitute a new temperature wall model, which we term a transformation-based wall model.

Finally, we examine the new temperature wall model *a posteriori* by applying it to our improved Baldwin–Lomax (BL) algebraic RANS model (Chen *et al.* 2024), as illustrated in figure 8. Since our focus is on temperature prediction, the so-called BL-GFM-VD model is selected as the benchmark one, which uses the GFM and VD (van Driest 1951) velocity transformations for improved scalings of the inner- and outer-layer eddy viscosity, respectively. On this basis, three models are compared: Model 1 does not use temperature wall models but prescribes $Pr_t = 0.9$ throughout (other choices of Pr_t have been discussed by Chen *et al.* (2024) and do not affect the main conclusions below); Model 2 uses (3.1) and (3.2) as the TV wall model; and Model 3 employs the transformation-based wall model instead. For the latter two models, the matching point is fixed at $y_m^* = 60$, to which $\bar{T}$ is not sensitive (Chen *et al.* 2024). The sampling point for Model 3 to compute $(\partial \bar{T}/\partial \bar{u})_w$ is selected to be $y^* = 80$, according to figure 9. The temperature prediction from these three models is compared with the DNS data in figure 10 for four severe cooling cases. A fifth case with a modestly cooled wall is also included, aiming to demonstrate that its higher prediction error of $(\partial \bar{T}/\partial \bar{u})_w$ than the severe cooling cases (see figure 9) has limited effects on the behaviour of Model 3. As discussed by Chen *et al.* (2024), the Model 1 results have obvious deviations from DNS for severe cooling cases even though the two velocity transformations have been incorporated, due to the rapid variation of Pr_t below the logarithmic region. Employing the TV wall model (Model 2) effectively improves the
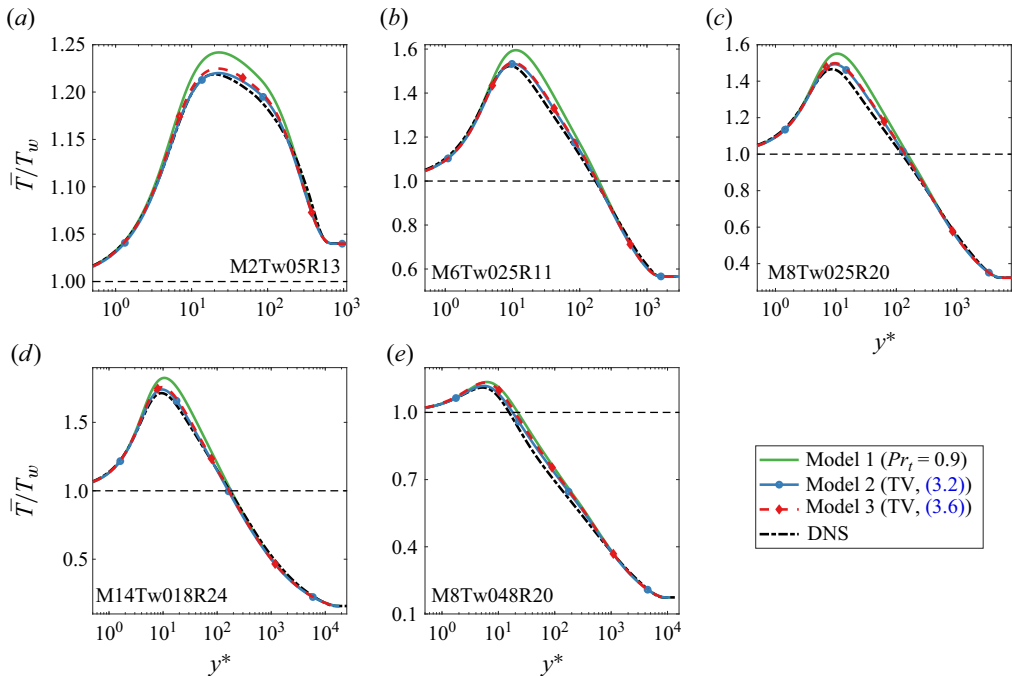
Figure 10. Temperature predicted by different Baldwin–Lomax models and from DNS for cases (*a*) VBL-M2Tw05R13, (*b*) ZDC-M6Tw025R11, (*c*) ZWLSL-M8Tw025R20, (*d*) ZDC-M14Tw018R24 and (*e*) ZDC-M8Tw048R20. The first four are severe cooling cases and the fifth one is a modest cooling case.

temperature prediction and attains close agreement with DNS for all the cases shown. The results between Models 2 and 3 are close to each other, proving that the transformation-based temperature wall model serves as an ideal alternative to the TV wall model and successfully excludes the dependence on boundary-layer-edge quantities.

4. Discussions and summary

4.1. *Discussions*

Zhang *et al.* (2014) derived and explained Pr_e as the effective Prandtl number. It is related to Pr_t as $Pr_e = Pr_t/(1 + \epsilon)$, where ϵ corresponds to the wall-normal eddy transport of the residual temperature fluctuation. This residual fluctuation can be difficult to obtain in simulations and measurements, so the interpretation and examination of Pr_e have to be made more from the mean flow perspective. In this work, we show that besides turbulence, Pr_e is also significant in determining $\bar{T}$ in laminar flows, which demonstrates that Pr_e is more fundamental than previous belief in describing the TV relation for compressible flows. In particular, the perfect collapse of Pr_e for laminar boundary layers over wide Ma_∞ and $T_w/\bar{T}_r$ ranges suggests that Pr_e serves as a robust modelling parameter, beneficial for constructing highly accurate laminar temperature models (figure 3).

This work also raises the significance of studying temperature transformations. A previous popular viewpoint is that temperature transformations are of limited interest for compressible turbulence modelling because the TV relation is already quite accurate. Nevertheless, as discussed in § 3, the TV relation is not closed by itself because it is derived from the analogy between the momentum and energy equations, while the analogy factor is left to be determined. Hence, the TV relation requires two outer boundary

conditions: one is the outer field samples $\bar{u}_m$ and $\bar{T}_m$ (not necessarily to be the edge; see (1.1) and (3.1)), and the other is the Reynolds analogy factor (3.2) which firmly relies on boundary layer edge quantities. This dependence on outer and edge values prevents the TV wall model from being a true self-determined inner-layer model, at least logically, and can obstruct its application to complex flow configurations. The combined strategy proposed in this work actually reaches a compromise between the inclosure of the TV relation and the inaccuracy of current temperature transformations. We anticipate more accurate temperature transformations in the future, which will help constitute a more solid inner-layer wall model, combined with velocity transformations.

Finally, from the turbulent results in §§ 2.4 and 2.5, we note that the near-wall r_g may serve as a means to examine the convergence of DNS data due to its high requirement to reach convergence. The velocity and temperature transformations can provide part of the theoretical foundation. Meanwhile, an important issue is raised to the community that a comprehensive examination is urgently required on the quality (convergence, spectral resolution, effects of numerical schemes, etc.) of established DNS datasets.

4.2. *Summary*

In this work, we revisit the compressible mean TV relation for both laminar and turbulent flows, considering both channels and boundary layers. A wide range of DNS datasets are employed for a comprehensive evaluation. We inspect two primary parameters, r_g and Pr_e, which are fundamental in the GRA deduced by Zhang *et al.* (2014) and in deriving the quadratic TV relation (1.1). Our efforts are on three aspects: explain the success of the TV relation where it works, improve its accuracy where it deviates and relax its limitation as a wall model by removing the dependence on boundary-layer-edge quantities.

The basic TV relations and related parameters turn out to be universal for the four configurations (§§ 2.2–2.5), indicative of some fundamental resemblance between laminar and turbulent flows. Common observations are summarised as follows. First, r_g is not a constant and has at least modest wall-normal variations in most cases, in contrast to the model assumption. Second, Pr_e is more critical than r_g in determining the shape of $\bar{T}$, and is less sensitive than r_g to flow conditions. Third, the sensitivity study designed on Pr_e is effective in explaining the success and failure of (1.1) in specific regions. For laminar channels, we show that (1.1) with fixed s is highly accurate at different Ma_b. For laminar boundary layers, we find that the quadratic TV relation has a systematic deviation (over-estimation) in temperature prediction, due to the systematic departure of Pr_e from unity. The $Pr_e^{-1}(\bar{u}/\bar{u}_e)$ turns out to exhibit a universal distribution irrespective of Ma_∞ and $T_w/\bar{T}_r$. Therefore, the prediction accuracy of $\bar{T}$ is significantly improved (figure 3) after introducing a curve fit of $Pr_e^{-1}(\bar{u}/\bar{u}_e)$, especially for cold-wall cases. The quadratic TV relation is generally accurate for turbulent boundary layers and channel flows, as widely reported before. Nevertheless, we note that Pr_e^{-1} has a modest systematic deviation from unity in the middle regime for channel cases, which results in modest temperature overprediction in that region; this overprediction can be reduced by using an improved description of Pr_e^{-1}. The velocity and temperature transformations can assist to understand the near-wall behaviour of r_g, which may also serve as a criterion to examine the convergence of DNS data.

Finally, we discuss the strategies to exclude the boundary-layer-edge quantities in turbulent temperature wall models. This is significant for expanding the applicability of the wall model because the boundary layer edge may not be easily determined in complex flows. The edge quantities are involved in the Reynolds analogy scaling to determine the wall boundary condition $(\partial \bar{T}/\partial \bar{u})_w$. As a means to exclude the dependence on the edge

quantities, we propose to employ the temperature transformation of Cheng & Fu (2024*a*) in the logarithmic region to close the TV relation. *A priori* examination using the DNS data proves that the temperature transformation can accurately recover $(\partial \bar{T}/\partial \bar{u})_w$ for cold-wall boundary layer cases. Moreover, *a posteriori* examination in our improved BL model demonstrates that the new transformation-based wall model can improve the mean flow prediction compared with those without temperature wall models (using prescribed Pr_t) for severe cooling cases ($\Theta < 0.2$), and it serves as an ideal alternative to the original TV wall model.

Future attention will be paid on possible extensions of the modified models to more complex configurations and their behaviours in the flows with moderate pressure gradients.

Appendix A. Derivations for laminar and turbulent boundary layers

First, we present the derivation of (2.11). Equation (2.10) can be rewritten as

$$-\frac{\Pi}{2} = (C_1 \bar{u}_\eta)_{\bar{u}} = \left(\frac{C_1}{\eta_{\bar{u}}}\right)_{\bar{u}}, \qquad \frac{1}{Pr}\left(\frac{C_1}{\eta_{\bar{u}}}\bar{T}_{\bar{u}}\right)_{\bar{u}} - \bar{T}_{\bar{u}}\left(\frac{C_1}{\eta_{\bar{u}}}\right)_{\bar{u}} + \frac{1}{c_p}\frac{C_1}{\eta_{\bar{u}}} = 0. \quad \text{(A1)}$$

Then, the coefficient $C_1/\eta_{\bar{u}}$ is solved as

$$\frac{C_1}{\eta_{\bar{u}}} = \frac{C_{1,w}}{\eta_{\bar{u},w}} - \frac{\Psi}{2} = \frac{\Psi_e - \Psi}{2}, \qquad \text{with } \Psi \equiv \int_0^{\bar{u}} \Pi \, d\bar{u}. \quad \text{(A2)}$$

As a result, the viscous parameters can be eliminated by substituting (A2) into (A1) as

$$(1 - Pr)\bar{T}_{\bar{u}}\Psi_{\bar{u}} = (\bar{T}_{\bar{u}\bar{u}} + Pr/c_p)(\Psi_e - \Psi). \quad \text{(A3)}$$

The wall boundary condition $\Psi_{\bar{u},w} = \Pi_w = 0$ leads to $\bar{T}_{\bar{u}\bar{u},w} = -Pr/c_p$, so (2.11) is arrived after a separation of variables. In addition, the perfect quadratic function $\bar{T}_{qd}(\bar{u})$ reads

$$\bar{T}_{qd}(\bar{u}) = T_w + \bar{T}_{\bar{u},w}\bar{u} + \frac{\bar{T}_{\bar{u}\bar{u},w}}{2}\bar{u}^2, \quad \text{(A4)}$$

which is subject to three wall boundary conditions $\bar{T}_{qd}|_w = T_w$, $\bar{T}_{qd,\bar{u}}|_w = \bar{T}_{\bar{u},w}$ and $\bar{T}_{qd,\bar{u}\bar{u}}|_w = \bar{T}_{\bar{u}\bar{u},w}$. As a result, the $\bar{Q}$-related expressions in (2.11) and (2.12) are obtained. Afterwards, the wall limit of r_g is derived. The numerator and denominator of (2.2*b*) and their first-order derivatives are all zero at the wall, so the wall limit is obtained by using L'Hôpital's rule twice, as $r_{g,w} = -c_p \bar{T}_{\bar{u}\bar{u},w}$, which simply equals to Pr.
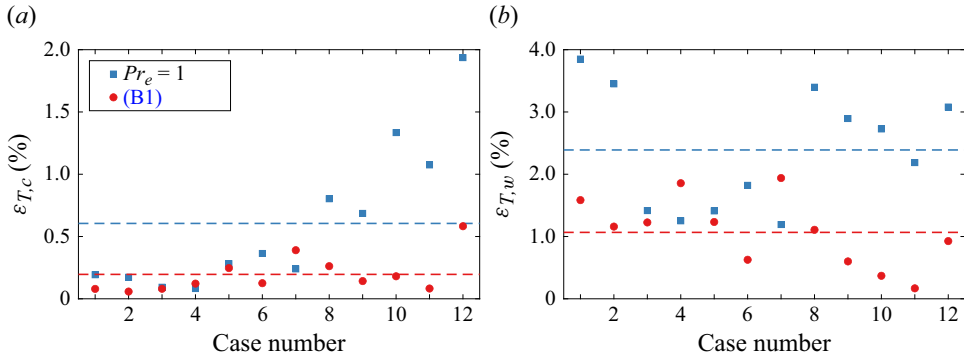
Figure 11. Relative error of the TV relations using different Pr_e models to the DNS data for turbulent channel cases: (*a*) error relative to $\bar{T}_{DNS}$, and (*b*) error relative to $(\bar{T}_{DNS} - T_w)$; see (B2*a,b*). The case numbers are defined in table 3. The horizontal dashed lines are the averaged errors of all cases.

The derivation of (2.16) is next presented. From (2.15), the first-order derivatives of $\bar{u}_{TL}^+$ and $\bar{\theta}_{SL}^+$ in the viscous sublayer are

$$\frac{\partial \bar{u}_{TL}^+}{\partial y^*} = \bar{\mu}^+ \frac{\partial \bar{u}^+}{\partial y^+} \approx 1 \approx \frac{1}{Pr} \frac{\partial \bar{\theta}_{SL}^+}{\partial y^*} = \frac{1}{Pr} \frac{\frac{y^+}{y^*}\sqrt{\bar{\rho}^+}\frac{\partial \bar{\theta}^+}{\partial y^+}}{1 - \frac{\bar{u}\bar{\tau}_w}{\bar{q}_w}}. \tag{A5}$$

As a result, (2.16) and $r_g = Pr$ are obtained after some simple algebra. This near-wall limit of r_g is the same as the laminar case. Similar derivations regarding the combination of velocity and temperature transformations were also provided by Chen *et al.* (2022*a*) for Couette flows, though they used Walz's equation instead of (1.1).

Appendix B. An improved fitting of Pr_e for turbulent channel flows

As discussed in § 2.5, an improved distribution of Pr_e can raise the accuracy of the TV relation for turbulent channel flows. Due to the scattering of Pr_e in figure 6(*b*) for different cases, an optimal model for Pr_e is not currently available. Therefore, we provide a simple curve fitting of the mean Pr_e^{-1} for these cases, as a demonstration of the possible strategies for model improvement. Using a third-order rational polynomial function, the mean Pr_e^{-1} is fitted as

$$Pr_e^{-1}\left(\frac{\bar{u}}{\bar{u}_c} \equiv x\right) = \frac{1 - \sum_{n=1}^{3} a_n x^n}{1 - \sum_{n=1}^{3} b_n x^n}, \quad \text{where} \begin{cases} a_1 = 3.605, \ a_2 = -4.432, \ a_3 = 1.826, \\ b_1 = 3.434, \ b_2 = -4.030, \ b_3 = 1.588. \end{cases} \tag{B1}$$

The fitted curve is plotted in figure 6(*b*) as the black dashed line for reference.

Now, the accuracy of two TV relations is compared: the first relation solves (2.4) with $Pr_e = 1$, leading to the quadratic relation (1.1); the second relation numerically solves (2.4) with (B1). Two types of errors are defined to measure their prediction accuracy relative to the DNS data:

$$\varepsilon_{T,c} = \frac{\int_0^{\bar{u}_c} |\bar{T}_{TV} - \bar{T}_{DNS}| \, \mathrm{d}\bar{u}}{\int_0^{\bar{u}_c} \bar{T}_{DNS} \, \mathrm{d}\bar{u}}, \qquad \varepsilon_{T,w} = \frac{\int_0^{\bar{u}_c} |\bar{T}_{TV} - \bar{T}_{DNS}| \, \mathrm{d}\bar{u}}{\int_0^{\bar{u}_c} (\bar{T}_{DNS} - T_w) \, \mathrm{d}\bar{u}}. \tag{B2a,b}$$

As shown in figure 6(*c*), the $\bar{T}$ variation relative to $\bar{T}_c$ is small for low-Ma_b cases, which may conceal the error of the TV relation, so the second type $\varepsilon_{T,w}$ is introduced for better inter-case comparisons. The distributions of $\varepsilon_{T,c}$ and $\varepsilon_{T,w}$ for the 12 cases in table 3, sorted

by Ma_b and Re_τ, are plotted in figure 11. As discussed above, $\varepsilon_{T,c}$ generally increases with the rise of Ma_b due to stronger $\bar{T}$ variations, whereas $\varepsilon_{T,w}$ is more uniform among cases and thus more strictly measures the errors at low Ma_b. Compared with the errors with $Pr_e = 1$, the Pr_e model (B1) reduces $\varepsilon_{T,c}$ and $\varepsilon_{T,w}$ in most cases, suggesting improved accuracy of the TV relation. As an overall measure, the mean $\varepsilon_{T,c}$ and $\varepsilon_{T,w}$ for all cases are reduced from 0.6 % and 2.4 % to 0.2 % and 1.1 %, respectively.

REFERENCES

ALCÁNTARA-Á VILA, F., HOYAS, S. & JEZABEL PÉREZ-QUILES, M. 2021 Direct numerical simulation of thermal channel flow for $Re_\tau = 5000$ and $Pr = 0.71$. *J. Fluid Mech.* **916**, A29.

BONS, J. 2005 A critical assessment of Reynolds analogy for turbine flows. *J. Heat Transfer* **127** (5), 472–485.

BRADSHAW, P. 1977 Compressible turbulent shear layers. *Annu. Rev. Fluid Mech.* **9** (1), 33–52.

BRADSHAW, P., HUANG, G.P. & LAUNDER, B.E. 1995 The law of the wall in turbulent flow. *Proc. R. Soc. Lond. Ser. A* **451** (1941), 165–188, 1941.

BUSEMANN, A. 1931 *Handbuch der Experimentalphysik*. Vol. **4**. Geest und Portig.

CHEN, P.E.S., HUANG, G.P., SHI, Y., YANG, X.I.A. & LV, Y. 2022*a* A unified temperature transformation for high-Mach-number flows above adiabatic and isothermal walls. *J. Fluid Mech.* **951**, A38.

CHEN, X., XI, Y., REN, J. & FU, S. 2022*b* Cross-flow vortices and their secondary instabilities in hypersonic and high-enthalpy boundary layers. *J. Fluid Mech.* **947**, A25.

CHEN, X., CHENG, C., FU, L. & GAN, J. 2023*a* Linear response analysis of supersonic turbulent channel flows with a large parameter space. *J. Fluid Mech.* **962**, A7.

CHEN, X., CHENG, C., GAN, J. & FU, L. 2023*b* Study of the linear models in estimating coherent velocity and temperature structures for compressible turbulent channel flows. *J. Fluid Mech.* **973**, A36.

CHEN, X., GAN, J. & FU, L. 2024 An improved Baldwin–Lomax algebraic wall model for high-speed canonical turbulent boundary layers using established scalings. *J. Fluid Mech.* **987**, A7.

CHENG, C., CHEN, X., ZHU, W., SHYY, W. & FU, L. 2024 Progress in physical modeling of compressible wall-bounded turbulent flows. *Acta Mech. Sinica* **40** (1), 323663.

CHENG, C. & FU, L. 2022 Large-scale motions and self-similar structures in compressible turbulent channel flows. *Phys. Rev. Fluids* **7** (11), 114604.

CHENG, C. & FU, L. 2023 Linear-model-based study of the coupling between velocity and temperature fields in compressible turbulent channel flows. *J. Fluid Mech.* **964**, A15.

CHENG, C. & FU, L. 2024*a* Mean temperature scalings in compressible wall turbulence. *Phys. Rev. Fluids* **9** (5), 054610.

CHENG, C. & FU, L. 2024*b* On the streamwise velocity, temperature and passive scalar fields in compressible turbulent channel flows: a viewpoint from multiphysics couplings. *J. Fluid Mech.* **983**, A38.

CHI, S.W. & SPALDING, D.B. 1966 Influence of temperature ratio on heat transfer to a flat plate through a turbulent boundary layer in air, In International Heat Transfer Conference. Begel House Inc.

COGO, M., BAÙ, U., CHINAPPI, M., BERNARDINI, M. & PICANO, F. 2023 Assessment of heat transfer and Mach number effects on high-speed turbulent boundary layers. *J. Fluid Mech.* **974**, A10.

COGO, M., SALVADORE, F., PICANO, F. & BERNARDINI, M. 2022 Direct numerical simulation of supersonic and hypersonic turbulent boundary layers at moderate-high Reynolds numbers and isothermal wall condition. *J. Fluid Mech.* **945**, A30.

CROCCO, L. 1932 Sulla trasmissione del calore da una lamina piana a un fluido scorrente ad alta velocita. *L'Aerotecnica* **12**, 181–197.

VAN DRIEST, E.R. 1951 Turbulent boundary layer in compressible fluids. *J. Aeronaut. Sci.* **18** (3), 145–160.

DUAN, L. & MARTÍN, M.P. 2011 Direct numerical simulation of hypersonic turbulent boundary layers. Part 4. Effect of high enthalpy. *J. Fluid Mech.* **684**, 25–59.

FU, L., KARP, M., BOSE, S.T., MOIN, P. & URZAY, J. 2021 Shock-induced heating and transition to turbulence in a hypersonic boundary layer. *J. Fluid Mech.* **909**, A8.

GIBIS, T., SCIACOVELLI, L., KLOKER, M. & WENZEL, C. 2024 Heat-transfer effects in compressible turbulent boundary layers – a regime diagram. *J. Fluid Mech.* **995**, A14.

GRIFFIN, K.P., FU, L. & MOIN, P. 2021*a* General method for determining the boundary layer thickness in nonequilibrium flows. *Phys. Rev. Fluids* **6** (2), 024608.

GRIFFIN, K.P., FU, L. & MOIN, P. 2021b Velocity transformation for compressible wall-bounded turbulent flows with and without heat transfer. *Proc. Natl Acad. Sci. USA* **118** (34), e2111144118.

GRIFFIN, K.P., FU, L. & MOIN, P. 2023 Near-wall model for compressible turbulent boundary layers based on an inverse velocity transformation. *J. Fluid Mech.* **970**, A36.

HASAN, A.M., LARSSON, J., PIROZZOLI, S. & PECNIK, R. 2024 Estimating mean profiles and fluxes in high-speed turbulent boundary layers using inner/outer-layer scalings. *AIAA J.* **62** (2), 848–853.

JIMÉNEZ, J., HOYAS, S., SIMENS, M.P. & MIZUNO, Y. 2010 Turbulent boundary layers and channels at moderate reynolds numbers. *J. Fluid Mech.* **657**, 335–360.

KADER, B.A. 1981 Temperature and concentration profiles in fully turbulent boundary layers. *Intl J. Heat Mass Transfer* **24** (9), 1541–1544.

MO, F. & GAO, Z. 2024 A new wall function method for hypersonic laminar boundary layers. *J. Fluid Mech.* **981**, A9.

MODESTI, D. & PIROZZOLI, S. 2019 Direct numerical simulation of supersonic pipe flow at moderate Reynolds number. *Intl J. Heat Fluid Flow* **76**, 100–112.

PASSIATORE, D., SCIACOVELLI, L., CINNELLA, P. & PASCAZIO, G. 2022 Thermochemical non-equilibrium effects in turbulent hypersonic boundary layers. *J. Fluid Mech.* **941**, A21.

PATEL, A., BOERSMA, B.J. & PECNIK, R. 2017 Scalar statistics in variable property turbulent channel flows. *Phys. Rev. Fluids* **2** (8), 084604.

PIROZZOLI, S. & BERNARDINI, M. 2011 Turbulence in supersonic boundary layers at moderate Reynolds number. *J. Fluid Mech.* **688**, 120–168.

PIROZZOLI, S. & BERNARDINI, M. 2013 Probing high-reynolds-number effects in numerical boundary layers. *Phys. Fluids* **25** (2), 021704.

SONG, Y., ZHANG, P., LIU, Y. & XIA, Z. 2022 Central mean temperature scaling in compressible turbulent channel flows with symmetric isothermal boundaries. *Phys. Rev. Fluids* **7** (4), 044606.

SONG, Y., ZHANG, P. & XIA, Z. 2023 Predicting mean profiles in compressible turbulent channel and pipe flows. *Phys. Rev. Fluids* **8** (3), 034604.

SUBBAREDDY, P. & CANDLER, G. 2012 DNS of transition to turbulence in a Mach 6 boundary layer. In *43rd AIAA Thermophysics Conference.* AIAA.

TRETTEL, A. & LARSSON, J. 2016 Mean velocity scaling for compressible wall turbulence with heat transfer. *Phys. Fluids* **28** (2), 026102.

VOLPIANI, P.S., BERNARDINI, M. & LARSSON, J. 2018 Effects of a nonadiabatic wall on supersonic shock/boundary-layer interactions. *Phys. Rev. Fluids* **3** (8), 083401.

VOLPIANI, P.S., BERNARDINI, M. & LARSSON, J. 2020 Effects of a nonadiabatic wall on hypersonic shock/boundary-layer interactions. *Phys. Rev. Fluids* **5** (1), 014602.

WALZ, A. 1969 *Boundary Layers of Flow and Temperature*. MIT press.

WENZEL, C., GIBIS, T. & KLOKER, M. 2022 About the influences of compressibility, heat transfer and pressure gradients in compressible turbulent boundary layers. *J. Fluid Mech.* **930**, A1.

WHITE, F.M. 1974 *Viscous Fluid Flow*. McGraw-Hill.

YAO, J. & HUSSAIN, F. 2020 Turbulence statistics and coherent structures in compressible channel flow. *Phys. Rev. Fluids* **5** (8), 084603.

ZHANG, C., DUAN, L. & CHOUDHARI, M.M. 2018 Direct numerical simulation database for supersonic and hypersonic turbulent boundary layers. *AIAA J.* **56** (11), 4297–4311.

ZHANG, P.-J.-Y., WAN, Z.-H., LIU, N.-S., SUN, D.-J. & LU, X.-Y. 2022 Wall-cooling effects on pressure fluctuations in compressible turbulent boundary layers from subsonic to hypersonic regimes. *J. Fluid Mech.* **946**, A14.

ZHANG, Y.-S., BI, W.-T., HUSSAIN, F. & SHE, Z.-S. 2014 A generalized Reynolds analogy for compressible wall-bounded turbulent flows. *J. Fluid Mech.* **739**, 392–420.